APPENDIX A

Pre-processing of the Free-Air Gravity Anomalies (FAGA)

A.1 Data Description

A FAGA grid has been determined by the National Imagery and Mapping Agency (NIMA) for the Greenland area (58.7 - 84.2°N and 285.75 - 349.50°E). The data used to generate this grid originate from several surveys, including observations processed by Brozena [1995] for the Naval Research Laboratory for the Greenland Aerogeophysical Projects of 1991 and 1992 (GAP91 and GAP92). These data were collected over the central ice-covered region, above the coastal areas and out approximately 100 km offshore with an average trackline spacing of 30 km. Because these data have not been widely distributed and used in many previous investigations, they offer a real possibility for examining heretofore unknown aspects of a remote region of the Earth.

NIMA used least squares collocation on terrestrial, marine and airborne gravity observations to generate 5 arcminute grids of FAGA values (Figure A.1) and observation errors (Figure A.2) at the respective elevations (Figure A.3) for each grid point (Forsberg and Kenyon, 1995). Predictions were made on this digital elevation model (DEM) to facilitate comparisons with surface control measurements.

Examination of Greenland's coastal regions in Figure A.1 shows the severe effects of these data being located upon the varying surface defined in Figure A.3. The FAGA field contains broader longer wavelength features over the smoother, central,

ice-covered regions and shorter wavelength features nearer the coasts and the edge of the ice sheet. This in part may be due to the further distance between the observation levels and subglacial crustal sources for the interior region as compared to the coastal regions.

The errors associated with these measurements indicate a high degree of confidence for those portions of the grid that are onshore or over enclosed waterways such as the Labrador Straits. Most of the areas containing larger observation errors are confined to the offshore regions of Northeast and Southeast of Greenland (Figure A.2).

For the purposes of this analysis, it is necessary to have all values at a uniform elevation and not on the DEM's surface. This will facilitate potential field analysis by removing terrain effects and emphasizing the remaining FAGA components.

It is also desirable to have the FAGA values sufficiently high enough above the nodes used by Gaussian Legendre Quadrature integration (GLQ) to optimize the accuracy of the inversion. In GLQ, prisms of material determined from a DEM are modeled to determine their gravity effects. For each prism, densities are assigned to several nodes to emulate the gravity effect of the entire prism. If the nodes are to close to the regions where gravity predictions are desired, singularities may develop that would inhibit the total calculation.

Finally, the desired data spacing for grids was selected at 6' (latitude) by 15' (longitude) grid or about 10 km by 10 km. This gridding interval was based upon the average data spacing for observed gravity data sets, as well as the intervals of other data set to which these gravity data will be directly or indirectly compared (magnetic data, altimeter-derived FAGA, and terrain DEM's).

A.2 Upward Continuation

An ideal elevation would be double the selected data spacing or about 20 km. The original FAGA grid (Figure A.1) had been downward continued from aircraft elevations to the DEM surface (Figure A.3) using GEOFOUR software developed by the authors of the original FAGA data [Forsberg and Kenyon, 1995]. Therefore, these data were now upward continued to 20 km using the same software (Figure A.4). This would result in wavelengths below 20 km being de-emphasized and the power of the remaining signal lowered to emulate the effects of data being observed further above the source region inside the Earth.

The energy of the upward-continued data (26 mgals) can be seen to be two thirds of the original data (39 mgals). Therefore, I assume that no serious degradation in the information contained in the upward-continued data has occurred. Examination of Figure A.1 and Figure A.4 shows that they essentially contain the same intermediate and longer wavelength information (CC=0.87). Gravity data for the offshore regions in Figure A.1 were originally at 0 km elevation, therefore, they may be of use later when examining smaller offshore features.

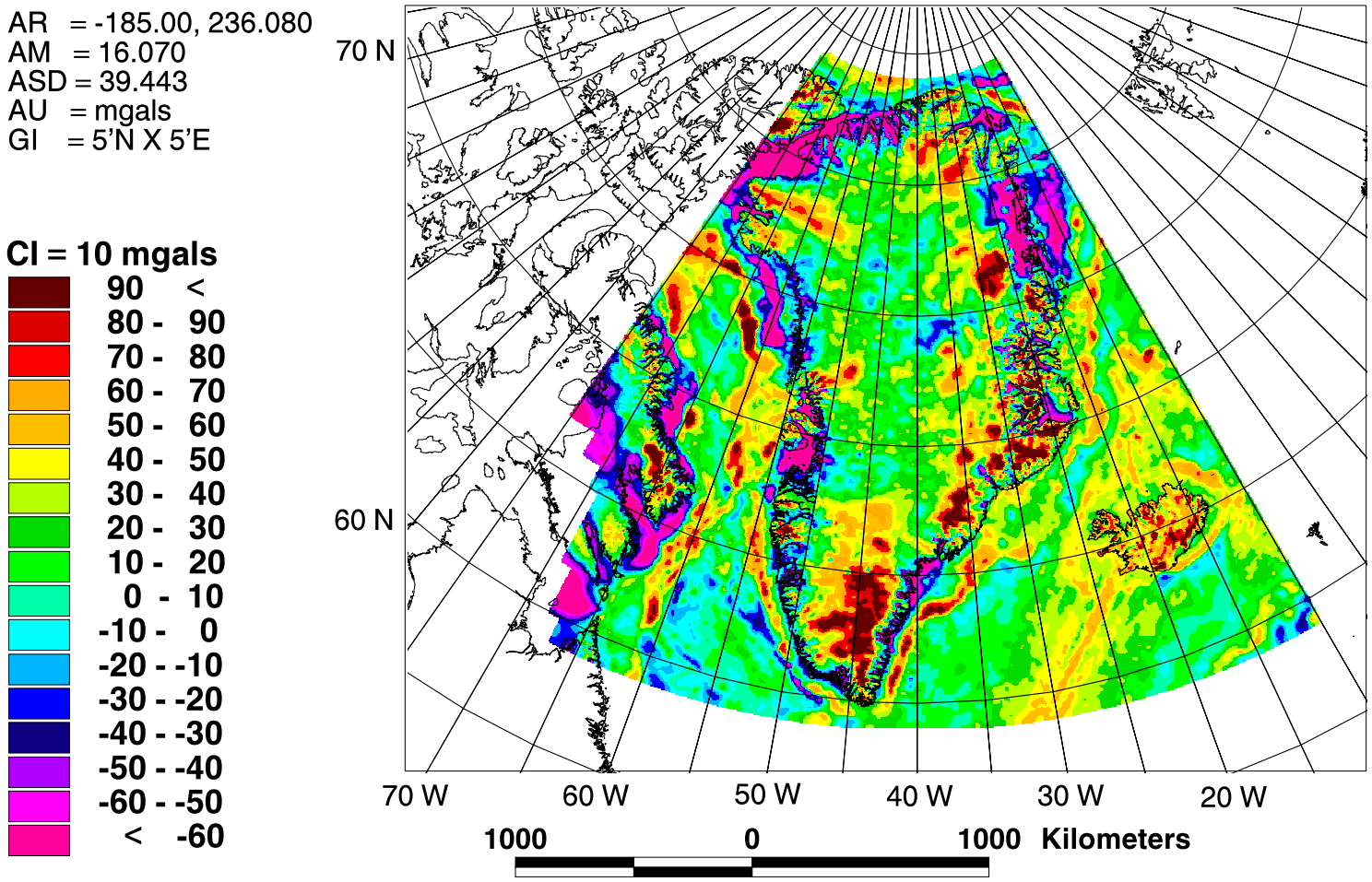

Figure A.1: Original NIMA Free-Air Gravity Anomalies (FAGA) at the Earth's surface shown in a Lambert Equal-Area Azimuthal Projection centered on 40 W. Data are registered to variable surface elevations that are given in Figure A.3.

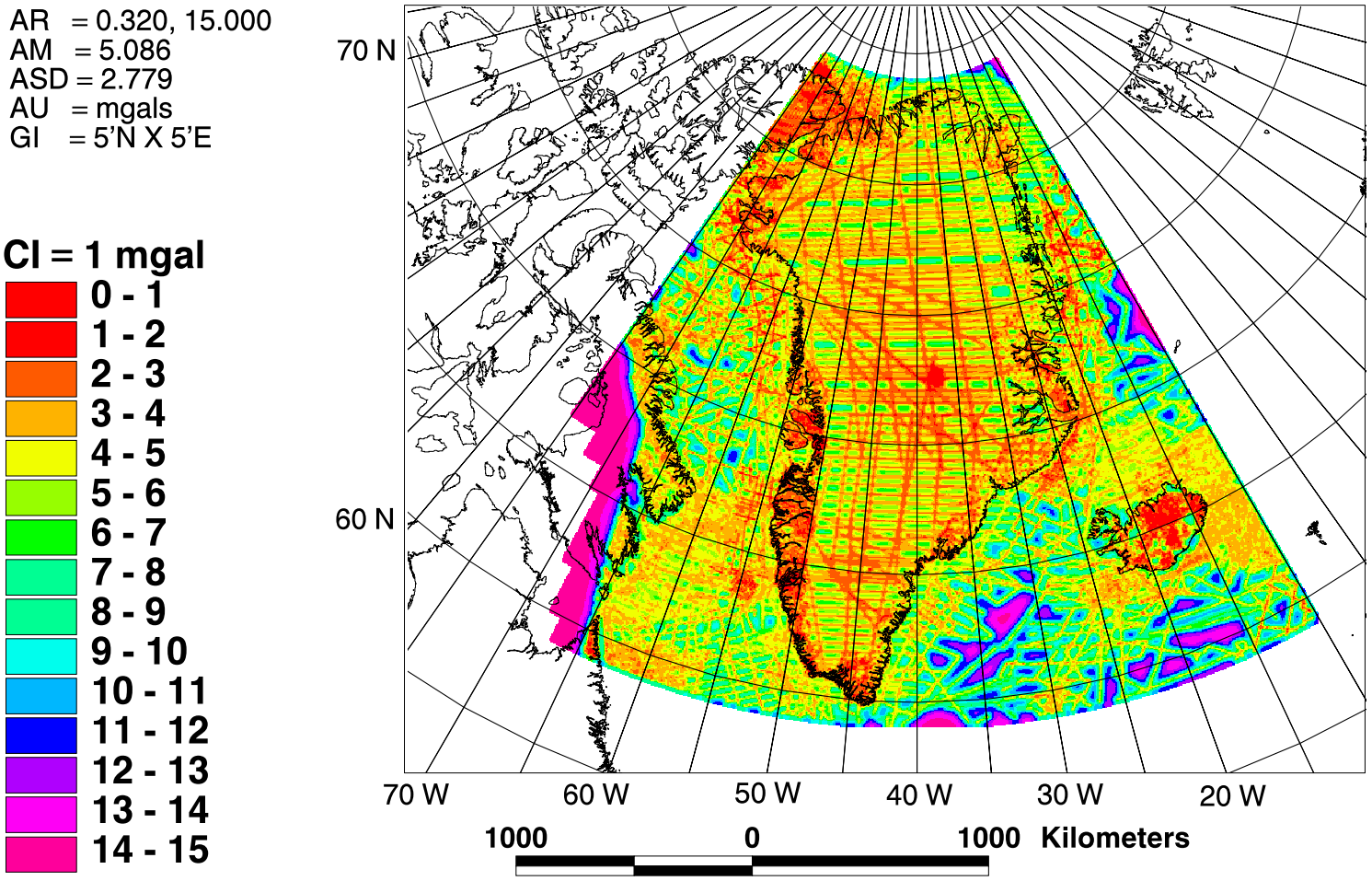

Figure A.2: Observation errors provided with the NIMA FAGA shown in a Lambert Equal-Area Azimuthal Projection centered on 40 W.

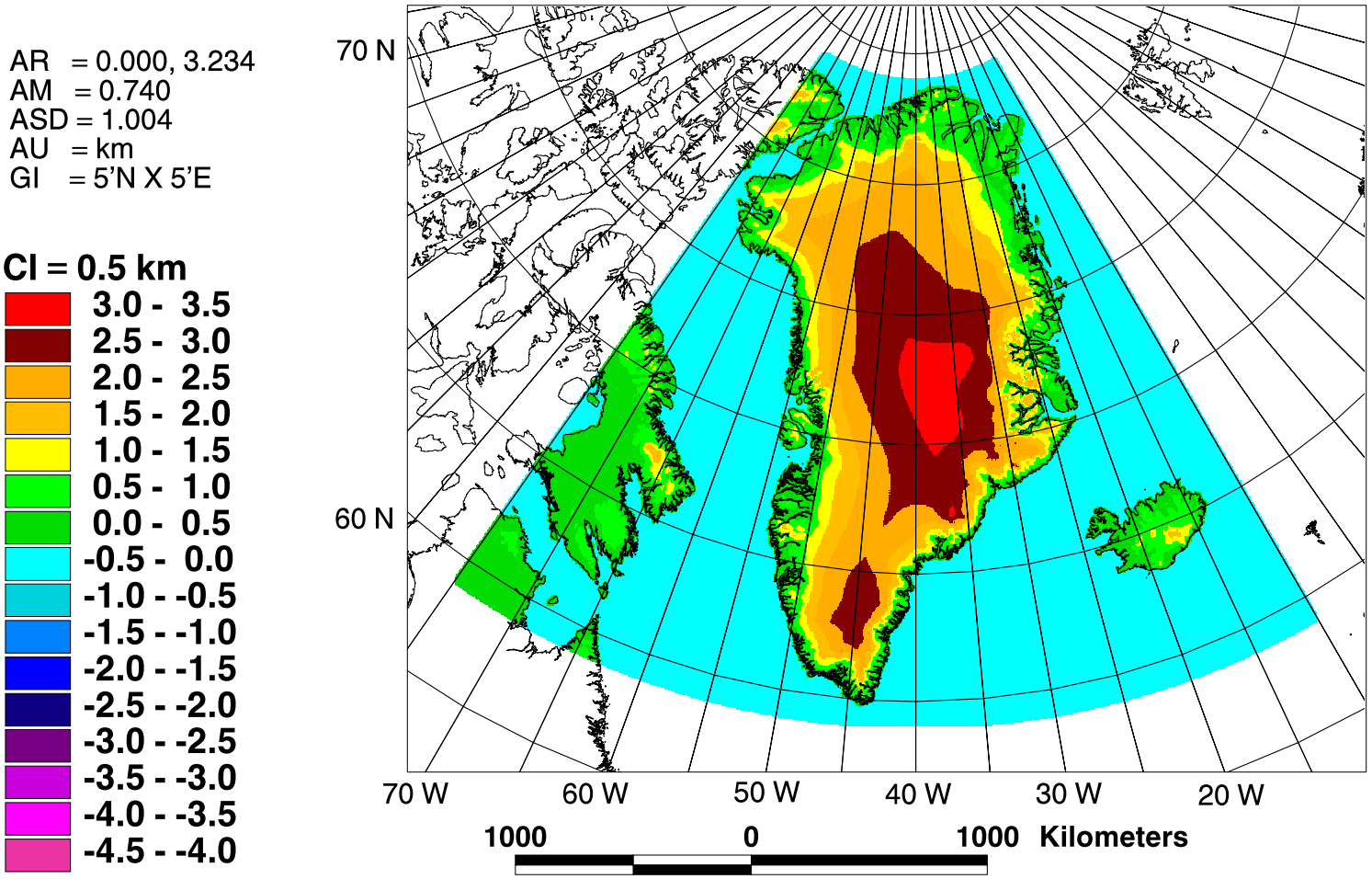

Figure A.3: Orthometric heights associated with the NIMA FAGA above mean sea level shown in a Lambert Equal-Area Azimuthal Projection centered on 40 W.

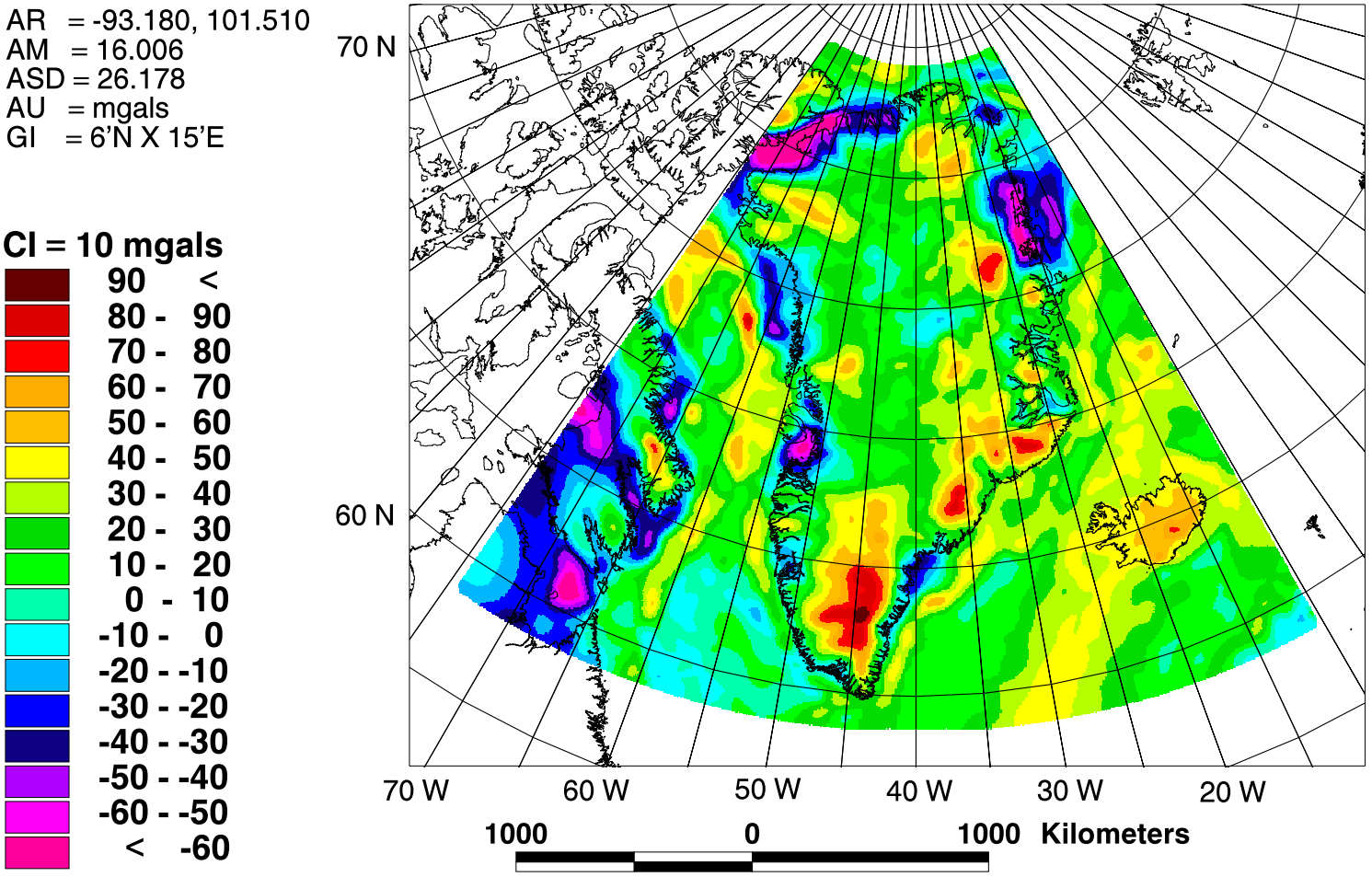

Figure A.4: NIMA FAGA upward continued to Z=20 km elevation shown in a Lambert Equal-Area Azimuthal Projection centered on 40 W.

APPENDIX B

Pre-processing of the Magnetic Anomalies (MA)

B.1 Data Description

The Geological Survey of Canada (GSC) compiled magnetic anomaly (MA) information (Figure B.1) in open file 3125b [Verhoef et al., 1996]. These data cover the entire Arctic and North Atlantic region in a 5 km grid, including the Greenland area (58.7 -84.2° N and 285.75 - 349.50° E). These data were derived from three general sources of data: shipborne, airborne, and prior gridded data sets. Shipborne data from several different surveys on both the North Atlantic and the East and West coasts of Greenland were merged to produce one major data set. Another major data set was derived from numerous airborne surveys covering Iceland and Greenland, including data collected by Brozena [1995] for the Naval Research Laboratory (NRL) during the Greenland Aerogeophysical Projects of 1991 and 1992 (GAP91 and GAP92). Additional airborne surveys covered the western Arctic Ocean and the Grand Banks. The final source of data derived from several previously gridded surveys covering the eastern Arctic Ocean and most other land areas, including Eurasia and North America.

Extensive efforts were made to merge these disparate data sources into a cohesive data set. Each of the three subsets (ship, air, and grid) were independently merged and gridded. To facilitate merging these sources, high pass filtering at 400 km was

selected rather than trying to remove individual tilts and biases. Hence, the resulting grid is composed of 400 km and shorter wavelengths, although the taper of the filter passed wavelengths as long as 1000 km at a much reduced power. The final gridding was derived using minimum curvature from 7.5 million data points in all three major data sets.

Of all of these data, only a few represent that subset that directly influenced the MA determined for the Greenland field area. These included the GAP91 and GAP92 aeromagnetic data plus data derived primarily from the Danish Geological Survey over southern Greenland and off the East coast [Verhoef et al., 1996]. For deeper oceanic areas along the eastern and western coasts, shipborne measurements provide the primary sources. The only previously gridded data set that was included covered the Diskó Island region and was a 2 km grid taken from a Decade of North American Geology compilation.

The filtering at 400 km wavelength is still sufficient for a crustal analysis because crustal MA sources will have a shorter wavelength characteristic, which should be adequately reflected in the 400 km and shorter wavelength components. It is assumed that magnetic sources will originate above the Curie isotherm in either the oceanic crust (depths to 10 km) or continental crust (depths to 60 km) [Shive et al., 1992]. Below the Curie isotherm, the rocks become randomly magnetized and lose their magnetic characteristics. With sources no deeper than 60 km, the resulting MA will be characterized by wavelengths shorter than 400 km.

For broad, shallow source regions such as the Caledonian Orogeny, there may be some components that are longer than 400 km. Because the hi-pass filter taper passed wavelengths up to 1000 km, the longer wavelengths associated with these sources will have some expression in the final data.

B.2 Upward Continuation

The original MA (Figure B.1) were upward continued to 20 km elevation (Figure B.2) for several reasons. The upward continuation was necessary because when GSC merged all the data into the final grid, the various data sets were merged at the elevations provided and not reduced to a common elevation. Most airborne data were collected at elevations between 200 to 400 m with some values were around 1 and 4 km, while shipborne observations were all at sea level. The gridded data were derived primarily from other aeromagnetic surveys occurring at varying elevations that were typical of those for the above airborne surveys. The aeromagnetic data used for these gridded data sets were not included with the other airborne data sources and do represent separate data.

Amplitudes may vary from one region to the next because of these significant differences in observation elevations. Upward continuation to 20 km will help to deemphasize these contrasts as 20 km is much greater than any of the elevations at which the various airborne, shipborne or gridded data were determined. The value of 20 km was selected to facilitate comparison with the 20 km upward continued FAGA data via Poisson's Relation. By placing both data sets at the same elevation, the radial derivative of the FAGA may be used to generate pseudo-magnetic anomalies for comparison with the MA. The FAGA data had been upward continued to 20 km to place them sufficiently above its source region.

B.3 Reduction to Pole

To be useful for comparison to the FAGA, the MA data must be effectively reduced to the magnetic pole. MA sources react to the Earth's magnetic field to generate the observed MA data. The MA can be broken down into three components: two horizontal and one vertical. Sources located at the geomagnetic poles will have only

a vertical field present. For comparison with FAGA data, which is oriented vertically, the MA data for all points must be reduced as if it were being observed at the geomagnetic pole, or reduced-to-pole (RTP).

This may be easily accomplished spectrally for uniform magnetic inclination and declination [Alsdorf et al., 1994]. However, a bulk of the data were collected over a 20 year span between 1970 and 1990 during which the corefield changed over time.

The International Geomagnetic Reference Field (IGRF) models provide references for the Earth's magnetic field components (declination, inclination, and intensity) at 5 year intervals. Figure B.3 was compiled by averaging the declination, inclination, and intensity values generated from the IGRF models for epochs 1970, 1975, 1980, 1985, and 1990.

During the 20 year span, the declination was characterized by a RMS difference of 1.1° and the inclination was characterized by a RMS difference of 0.1°. These are relatively small compared to the magnitude of the average declination and inclination values found within the field area (Figure B.3). Therefore, the effects caused by the changing corefield over time will be assumed negligible compared to the magnitude of the differences obtained by comparing one portion of the field area against another. As an example, the declination varies from $-15°$ in the Southeast to $-90°$ in the Northwest. This is an order of magnitude greater than the 1.1° RMS difference.

Therefore, the averages given in Figure B.3 were utilized as the basis for further modeling the RTP process for this region. The approach that was selected for performing the reduction-to-pole for the entire MA data set required the subsetting of the region into 4 corners and the central region. Inclination and declination pairs were selected and are given in Table B.1.

Selection of five points to perform this adjustment was based upon the rapidity of the change away from one corner to the next. Values within about 700 km ($6.3°N$

Location	Latitude (°N)	Longitude (°W)	Inclination (°)	Declination (°)
Southwest	61.800	66.500	-38.81	81.16
Northwest	81.000	66.500	-78.36	86.22
Northeast	81.000	18.500	-31.18	83.45
Southeast	61.800	18.500	-19.63	74.19
Central	71.350	42.625	-43.47	81.13

Table B.1: Inclination and declination pairs for reduction-to-pole. Values were selected at points inset from the four corners and at the middle of Figure B.3. The reduction-to-pole is performed for each of these pairs, and the procedure is assumed valid for approximately 700 km around each point. Values for points more than 700 km from these points represent a weighted average of the values generated by all the below pairs.

x 15.75°E) of each corner pair are assumed to be correctly reduced. Outside of that range, the selected pair may not provide an adequate reduction-to-pole. So values derived nearest each corner pair will be retained and the values in between must be a blend of values obtained from different corner pairs.

The 20 km upward-continued MA data were reduced-to-pole using the first 4 pairs given in Table B.1. The 6.3°N x 15.75°E patch around each pair was retained, and the remaining grid values in the overlapped regins were linearly merged. This was accomplished by weighting the values according to proximity to their source grid (i.e., if a point in question lies closer to one corner pair than another, then the value derived from the closest pair is given more weight than the value derived from the more distant pair).

For purposes of comparison, the central portion of this 4-pair adjusted MA grid was compared to values derived from the middle pair (last values in Table B.1). These data should be adequately adjusted in terms of proximity to the central pair. Therefore, comparison of the 4-pair adjusted core region with middle pair adjusted core region will enable an assessment of the errors involved in the linear merging

process. The values in the center of the 4-pair adjusted data are the furthest from all 4 corner pairs and would be the region having the highest probability of error.

Differencing these cores generates a residual field that is characterized by low power ($\sigma = 2.6$ nT), little bias ($\mu = 0.535$ nT), and small amplitudes (max/min=9.6/-14.0 nT). These results clearly indicate that the associated mismatches between these data are well within the observation errors given with these data, which range from 25 to 100 nT [Verhoef et al., 1996].

As a final step, the middle pair derived grid was also added to the overall grid. The final 5 pair adjusted grid retains the values within the range of $6.3°N$ x $15.75°E$ around each of the five points given in Table B.1) and the data between these 5 regions are linearly merged, weighting the values derived from the closest declination and inclination the highest.

These MA data (Figure B.4) have now been hi-pass filtered at 400 km wavelengths to remove biases and tilts, upward-continued to 20 km elevation to reduce the effects of varying observations, and effectively reduced-to-pole to reduce the dipolar effects of the Earth's magnetic field. The last aids in clarifying the location and nature of the magnetic anomaly source, a necessary step if these data are to be compared with the gravity data.

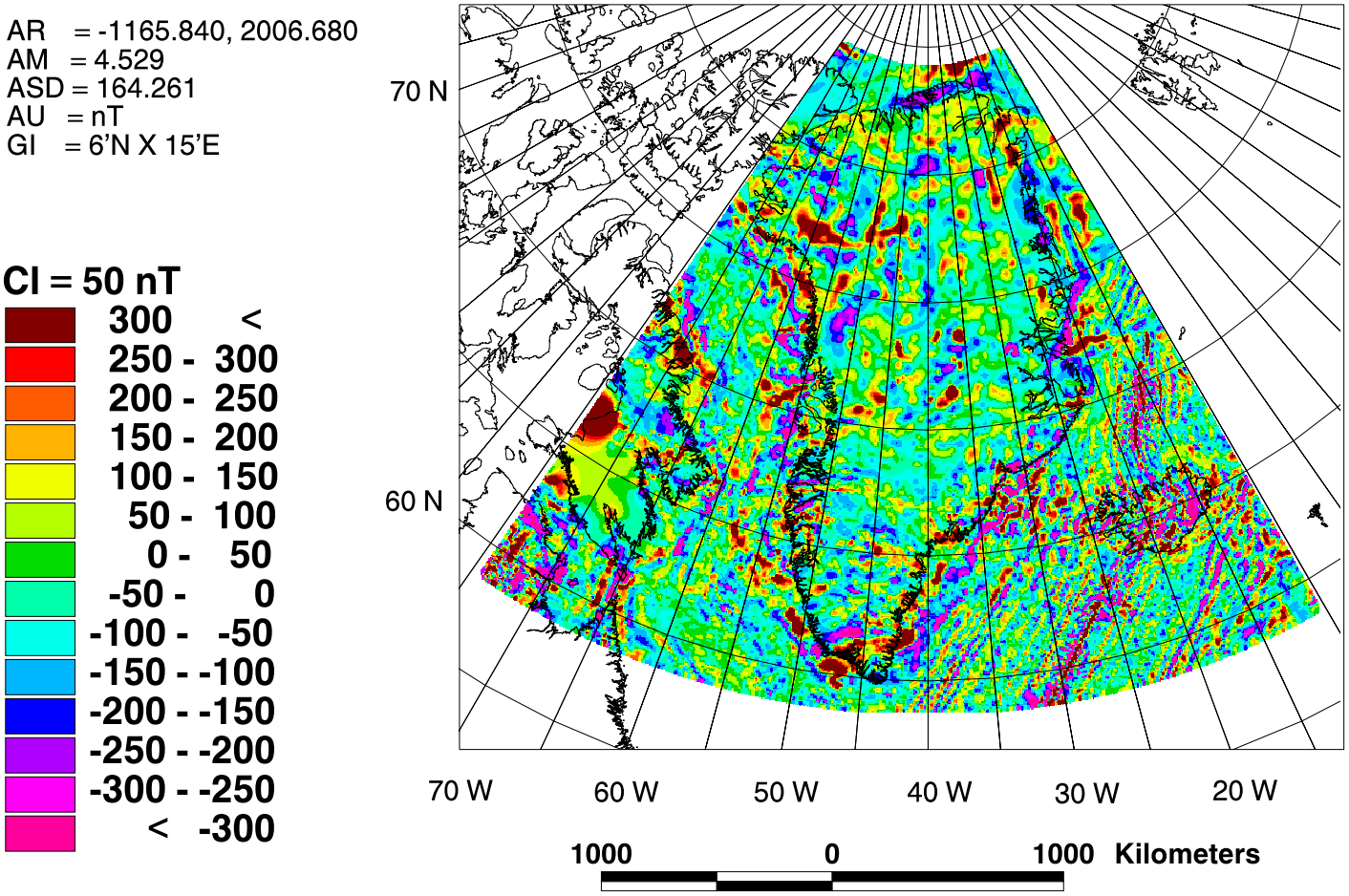

Figure B.1: Magnetic anomaly data provided by GSC from Open File 3125b for Greenland shown in a Lambert Equal-Area Azimuthal Projection centered on 40 W.

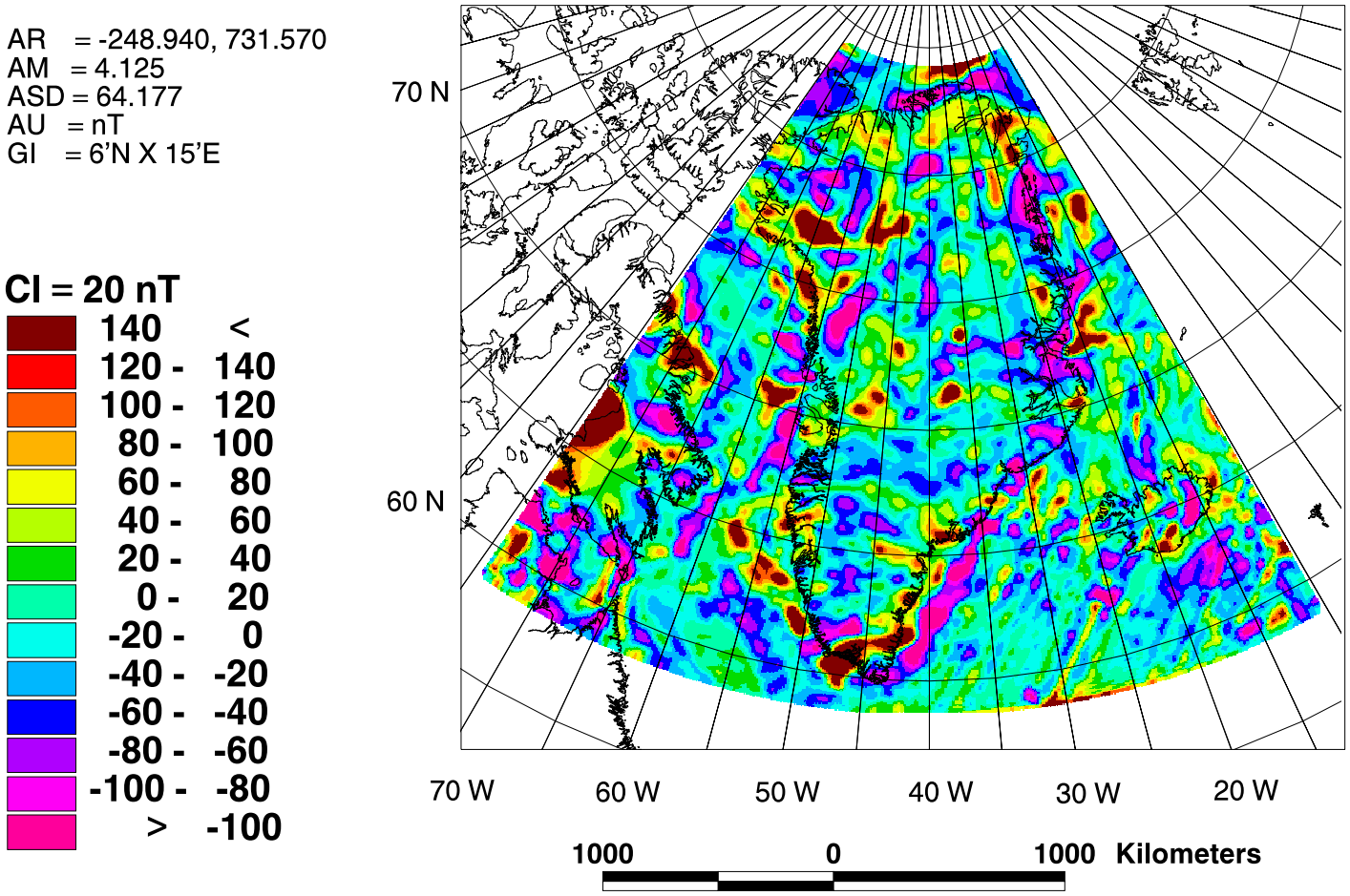

Figure B.2: Corrected magnetic anomaly data for Greenland shown in a Lambert Equal-Area Azimuthal Projection centered on 40 W. Data are reduced-to-pole to clarify the location of magnetic sources and are upward continued to 20 km elevation for comparison with gravity data.

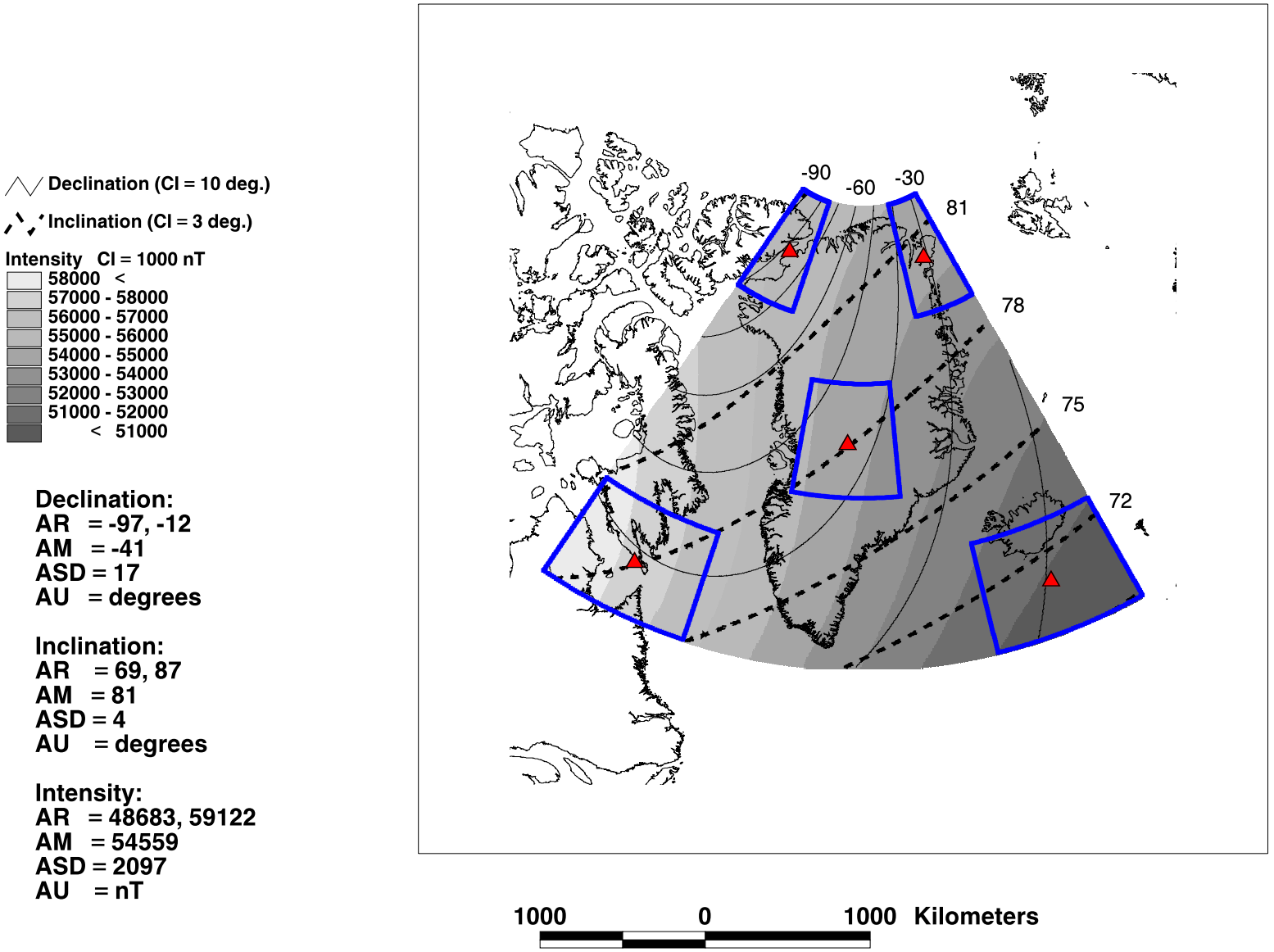

Figure B.3: Average IGRF derived Declination (solid line), Inclination (dashed line), and Intensity (grey scale) shown in a Lambert Equal-Area Azimuthal Projection centered on 40 W. Data were obtained and averaged from the 1 degree IGRF models for epochs 1970-1990. The graticule is left out for clarity.

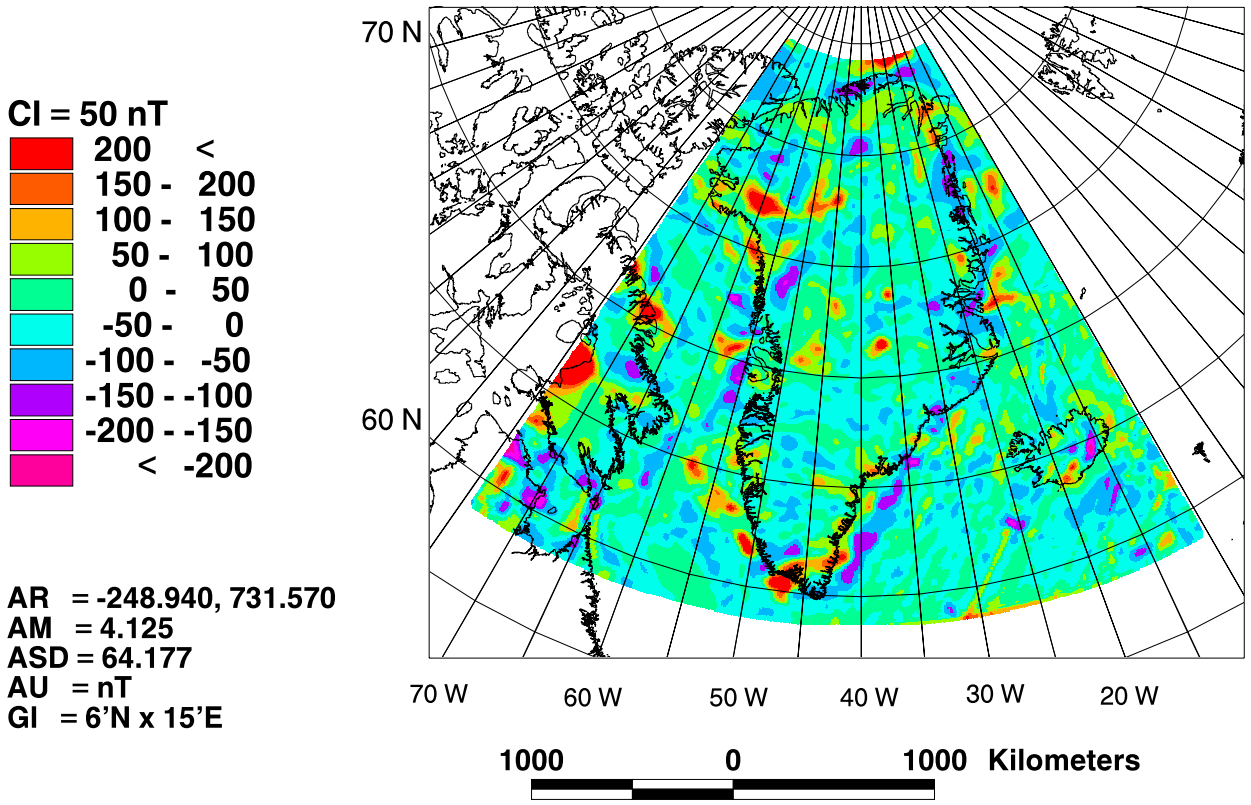

Figure B.4: MA reduced-to-pole and upward-continued to 20 km elevation shown in a Lambert Equal-Area Azimuthal Projection centered on 40 W.

APPENDIX C

Altimetry Enhanced Free-Air Gravity Anomalies

Abstract

The shortest wavelengths of ERS-1 altimeter data (168 day missions) are geographically ordered, and their common components extracted to generate an adjustment to a reference free-air gravity anomaly (FAGA) grid. Altimetry is residualized to a reference geoid surface generated by integrating the Andersen & Knudsen FAGA for the Barents Sea. Residuals for ascending and descending modes are processed separately. Track pairs in each mode are geographically ordered, transformed into the wave domain, and those wavelengths with the highest correlation and retained power are selected. These wavelengths, which should reflect common geological sources, are inversely transformed, averaged, and gridded. The two grids derived from each mode are merged to generate a final grid that has minimal trackline noise. This residual geoid surface is transformed into a residual FAGA surface, which is then merged with the original FAGA to generate the final altimetry enhanced FAGA. These enhanced FAGA have been checked in the Gulf of Mexico against high density observations and show a coherence of 50% down to 50 km wavelength. They may be averaged with other available data for a 50% coherence at 35 km, which is the optimum expected for Geosat altimetry in this region.

C.1 Introduction

Satellite altimetry has been used extensively to derive free-air gravity anomalies (FAGA) for all ice-free, ocean areas [Andersen and Knudsen, 1998; Kim, J.-H., 1995; Rapp and Yi, 1996; Rapp et al., 1991; Sandwell and Smith, 1997]. Each author has their own methodology that have resulted in different FAGA estimations using the same altimeter data sets.

Some criteria that authors use may eliminate or greatly reduce the weighting for altimeter measurements obtained to close to coastal areas or in shallower seas. This is based upon quality assessment of the altimetry under those conditions. Additionally, all available data sets have been incorporated into many of these analyses employing various weighting schemes to account for varying quality between data collected during different missions (Geosat, ERS-1, Topex, etc.).

These schemes often do not take into account the geologic sources that generate the FAGA signal. Primarily, the data are reduced based entirely upon a numeric approach. Therefore, an approach is offered here that assesses geographically adjacent profiles to determine the similar static components, which are assumed to derive from geological sources.

To that end, profiles that have the closest spacing between track are desired, because they will generate the best between track resolution (i.e., they could contain FAGA signals at double the spacing). Geosat altimetry from the GM mission has a much better between track spacing (3-4 km at the equator) than the combined ERS1 168-day missions (8 km at the equator). Therefore, it is desirable to use Geosat to estimate the shorter wavelengths of the Earth's gravity field and all available data for the longer wavelengths. However, Geosat altimetry extends only to $\pm 72^{\circ}$ latitude.

Therefore, the combined ERS-1 168 day missions were used, because they extend to $\pm 83°$.

These data must have the longer wavelengths removed, so that the shorter wavelengths may be processed to determine a residual FAGA field. This is practically accomplished by determining and removing a reference geoid undulation field. The residual profiles are then filtered to remove track noise, ordered geographically, and then spectrally compared to adjacent pairs.

Geologic sources that have a signal larger than the between track spacing of the altimetry should register on both tracks. Retention of this signal is critical to determining the high frequency component of the Earth's gravity field.

The original reference FAGA are enhanced by the addition of this residual field, because subtle features are restored that were masked or removed during the compilation of multiple altimetry sources. This added-value approach builds upon the remove-and-restore technique mentioned in Bašić and Rapp [1992]

C.2 Altimeter-Implied Free-Air Gravity Anomalies

There are two primary approaches to the generation of Free-Air gravity anomalies (FAGA) from altimeter data. Both rely upon the fact the ocean surface is a relatively good proxy indicator of the geoid undulation surface.

The first involves taking the along track derivative and interpolating this to intersection points to estimate the deflection of the vertical, which can be directly related to the desired FAGA [Sandwell and Smith, 1997]. The advantage to taking the along track derivative is that the long wavelength orbit errors are de-emphasized.

Another approach [Kim, 1993] uses the altimetry to directly calculate a geoid undulation and then determine the FAGA from the geoid surface. The inherent problem of orbit errors is reduced in the following two ways. The residual profiles are

geographically ordered and compared to extract the most correlative static elements, which are assumed to have common crustal sources [Kim, 1993]. This process is repeated for all pairs within each track mode (ascending and descending). The final two grids reflect residual orbit errors, as well as track noise.

The second means of reducing track noise is discussed in Kim et al., [1998]. In each grid, two quadrants will have minimal noise. Due to orthogonality, the quadrants with minimal noise for the grids derived from different modes will be opposite. Therefore, it is possible to retain the two least noisy quadrants from each grid's spectral amplitude plot and combine them into one spectrum. This may be inversely transformed to generate a merged geoid undulation that has minimal errors, which have been referred to as a corrugated [Verhoef et al., 1997] or washboard [Kim et al., 1998] effect.

The resulting geoid undulation grid is then used to generate the desired FAGA, essentially by taking the first vertical derivative. The advantage to this approach is that long wavelength errors are reduced first, then minimized further by taking the vertical derivative.

Additionally, in his approach, Kim [1993] removed the OSU91A geoid undulation values from the altimetry and later restored the OSU91A FAGA to the final grid of residual FAGA data that were derived from the residual altimetry. It has been previously shown [Rapp et al., 1991] that use of this remove and restore technique generates a valid solution.

The enhancement techniques discussed next are a variant on the second approach and are outlined in the flowchart in Figure C.1. The principle difference is that reference geoid and FAGA data are utilized, which have information at shorter wavelengths (down to 20 km) than those from 360 degree coefficient models.

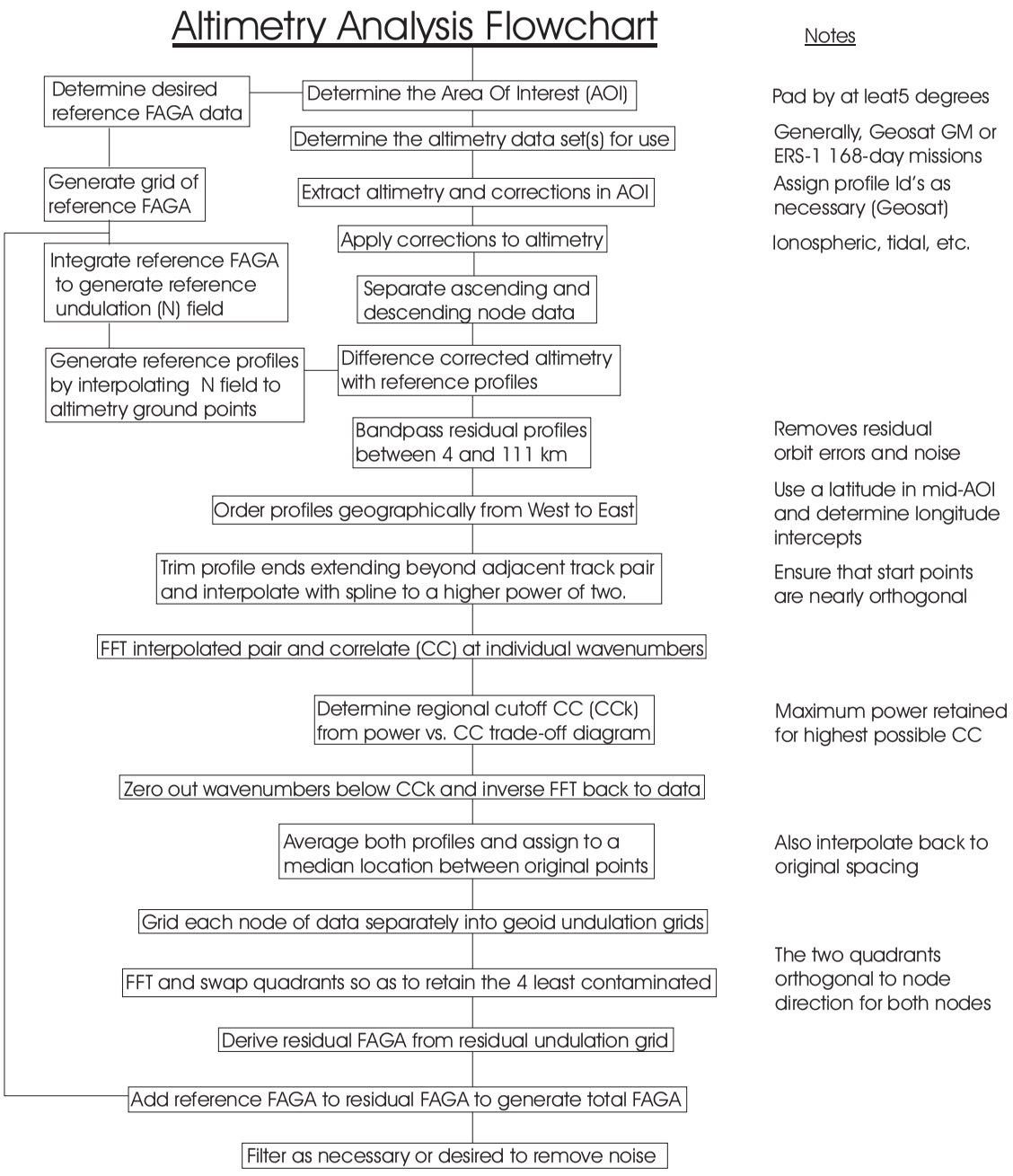

Figure C.1: Altimetry analysis flowchart. Various processing steps are necessary to generate enhanced FAGA. Ultimately, the long wavelength component of the reference FAGA data is combined with the short wavelength data from the altimetry.

C.3 A case study: The Barents Sea

A test area for this approach was selected in the Barents Sea. This region was selected because of sufficient ERS1 altimetry coverage (Figure C.2) for determining the high frequency component of the FAGA field. Additionally, it is also a continental shelf sea with shallow bathymetry that is likely to be well represented in the short wavelength features of the FAGA.

These techniques were implemented with altimetry from the ERS-1 168-day mission and a reference FAGA grid from Andersen and Knudsen [1998] (KAFAGA), which is shown in Figure C.3. There are some bias/tilt differences between KAFAGA data and other data sets [Smith, 1997], however, they do provide an excellent reference for FAGA data for the shorter wavelengths that are of primary interest here. KAFAGA was derived from multiple altimetry data sets, which have been shown to be reliable down to a range of 20 - 50 km wavelengths depending on location [Yale et al., 1995].

KAFAGA was used to generate a reference geoid undulation grid (Figure C.4) by use of a 2D FFT transform provided by Dru Smith of the National Geodetic Survey. Reference undulation profiles were generated by interpolating the reference undulation grid to the 1/10 second altimeter groundpoint locations. The top diagram in Figure C.5 shows a reference undulation profile (dashed) and an observed altimeter profile (solid) over the same groundpoints, and it can clearly be seen that there are long wavelength discrepencies between these two profiles, which may be attributed to residual orbit errors and tilt errors in the reference model. The bottom diagram in Figure C.5 shows that the differences are primarily long wavelength, along with spikes and very high frequency features. The latter may contain both observation noise and real signal. When the long wavelength differences and spikes were removed

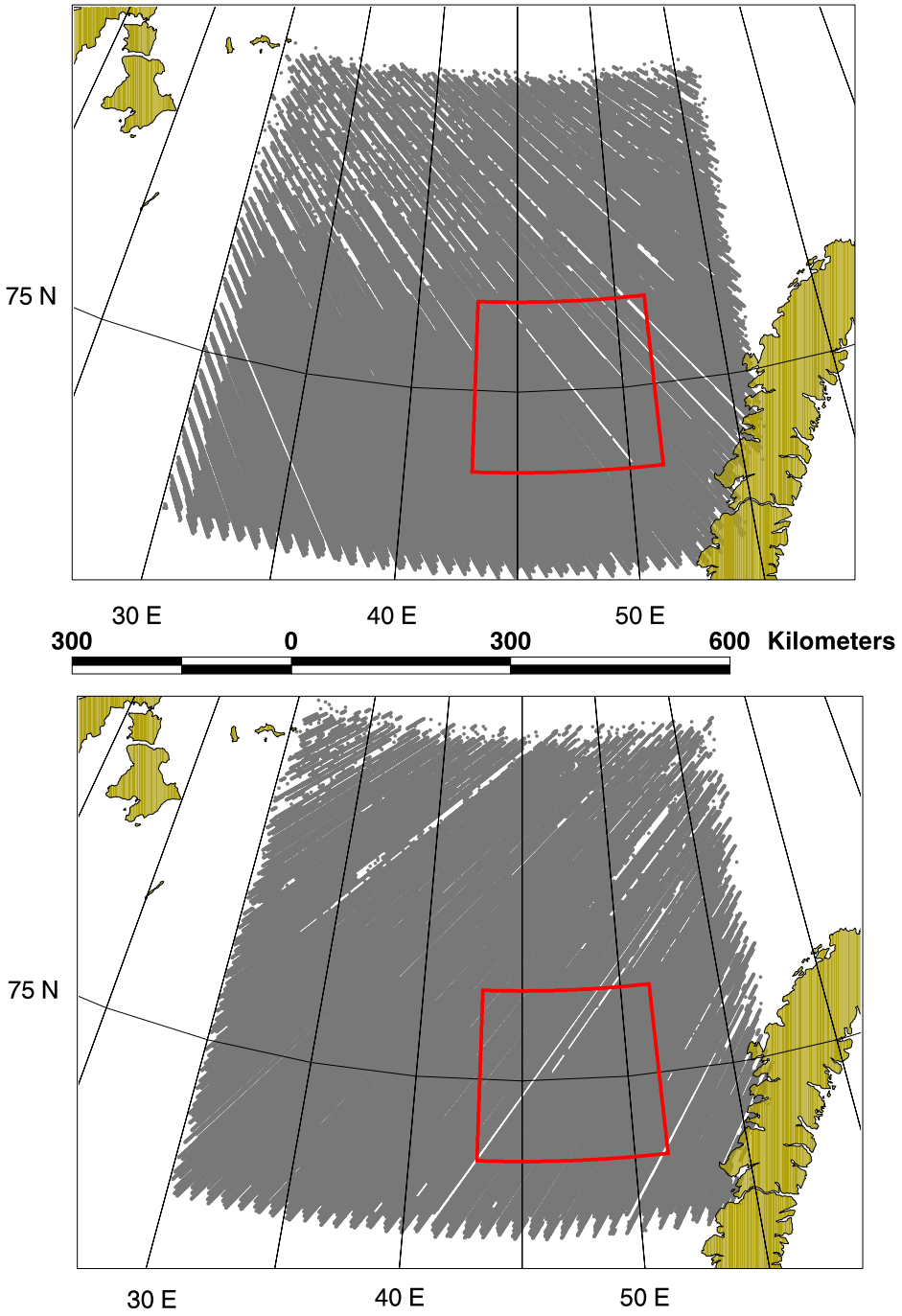

Figure C.2: 168-day ERS-1 altimetry for the Barents Sea. Ascending (top) and descending (bottom) altimeter coverage can be seen to be sufficient for the test area (red box) and is shown in a Lambert Equal-Area Azimuthal Projection centered on 45 E at sea level.

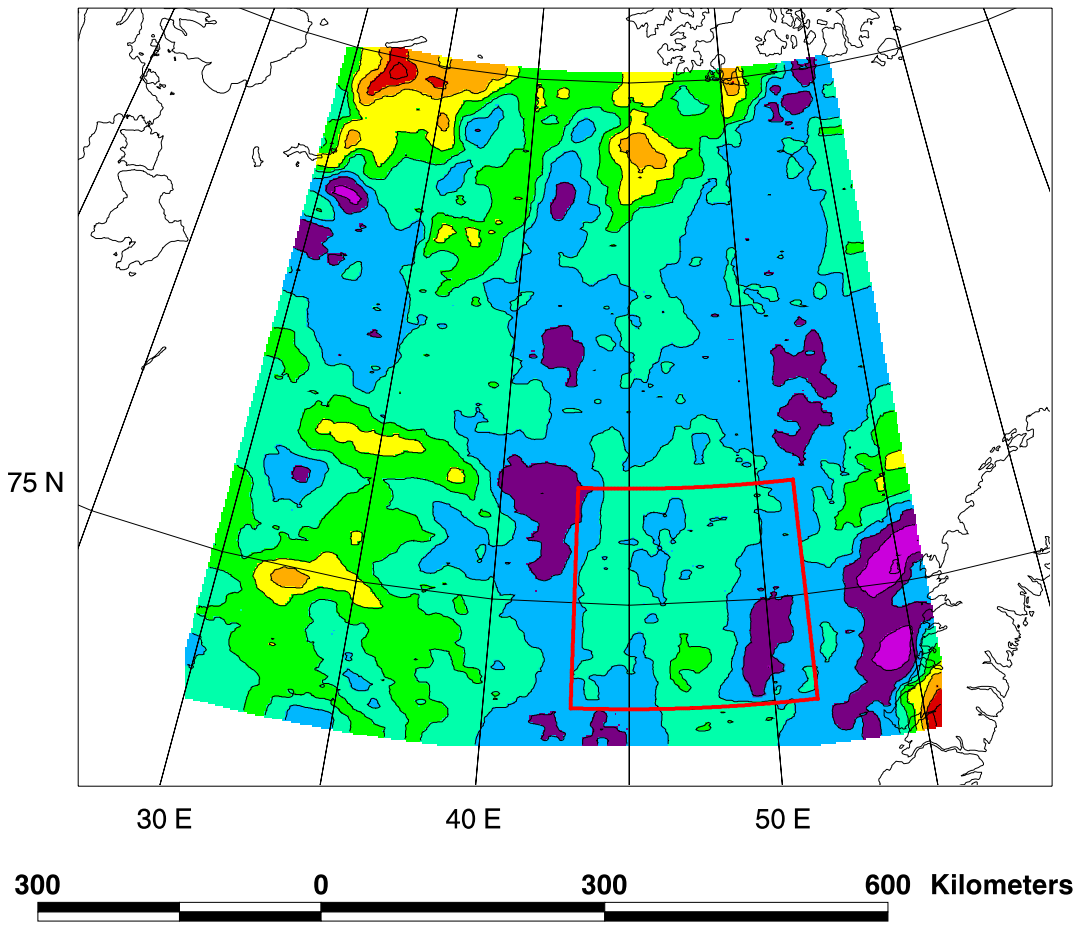

Figure C.3: Andersen and Knudsen FAGA for the Barents Sea shown in a Lambert Equal-Area Azimuthal Projection centered on 45 E at sea level. The test area is shown with the red box.

by filtering, the filter altimetry profile and the reference undulation profile were very correlative (CC=0.999) and had little RMS difference (0.036 m).

For this analysis, all differences greater than 111 km wavelength will be treated as orbit errors and filtered out. The intent here is to provide a more refined high frequency field that will better represent the short wavelength features associated with the sea bottom. Therefore, any long wavelength errors that may result from this assumption will have a negligible impact. Additionally, track spacing is generally 2 km or greater for this region. Since the distance between tracks controls the cross-track resolution while the 1/10 second sample interval (about 660 m) controls the along track resolution, the minimal resolution from these data is about 4 km.

The removal and restoration of a reference field closely follows the technique presented by Bašić and Rapp [1992]. They removed fields derived from spherical harmonic coefficients, whereas the models here are based directly upon observed data. The relationship of the geoid undulation field and the FAGA field are given through the fundamental equation of geodesy (Equation C.1)

$$\Delta g = -\frac{\partial T}{\partial r} - \frac{2T}{R} \tag{C.1}$$

where: Δg = free air gravity anomalies
T = disturbing potential
r = radial direction
R = mean Earth radius = 6371 km

and Bruns' Formula Equation C.2) [Heiskanen and Moritz, 1967]

$$T = N\gamma \tag{C.2}$$

where: N =geoid undulation
γ = normal gravity

A planar assumption is made based on the removal of the reference geoid, and a standard vertical derivative operator may be applied to the Fourier transform of the

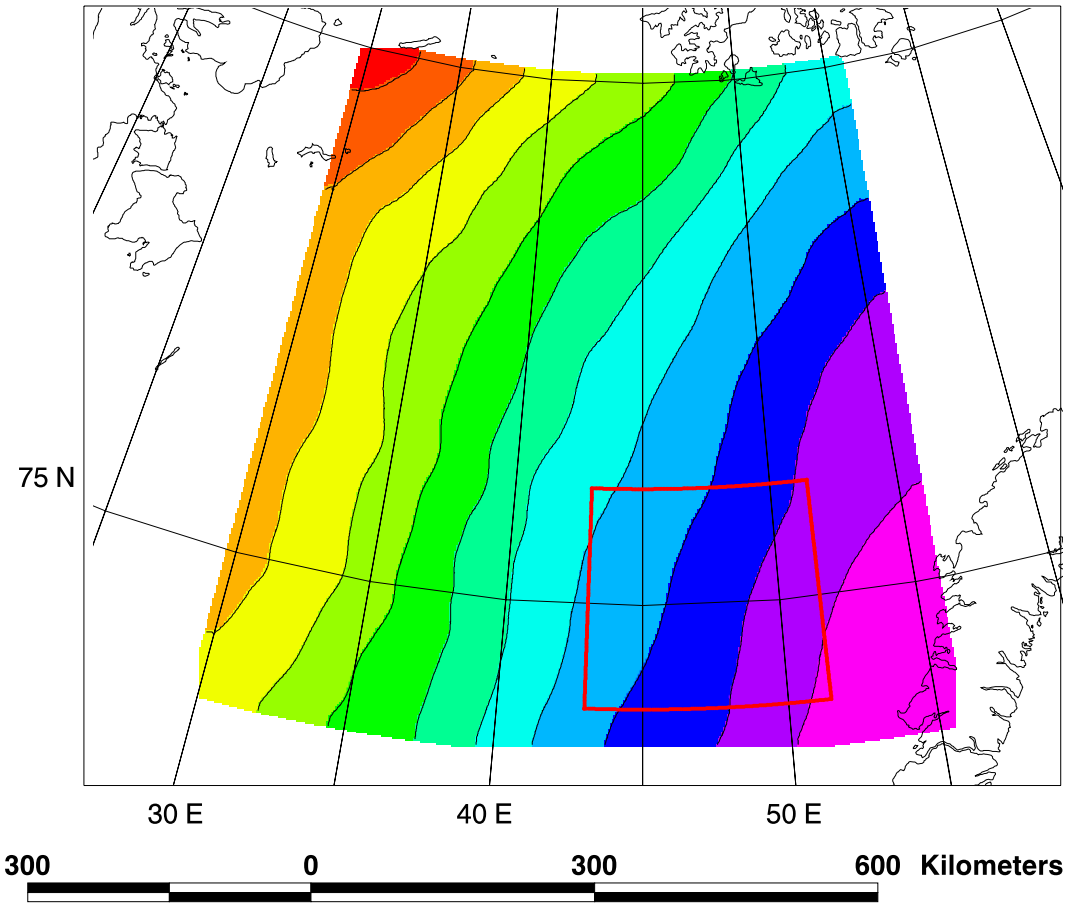

Figure C.4: Andersen and Knudsen FAGA-derived geoid undulations for the Barents Sea shown in a Lambert Equal-Area Azimuthal Projection centered on 45 E at sea level. The test area is shown with the red box.

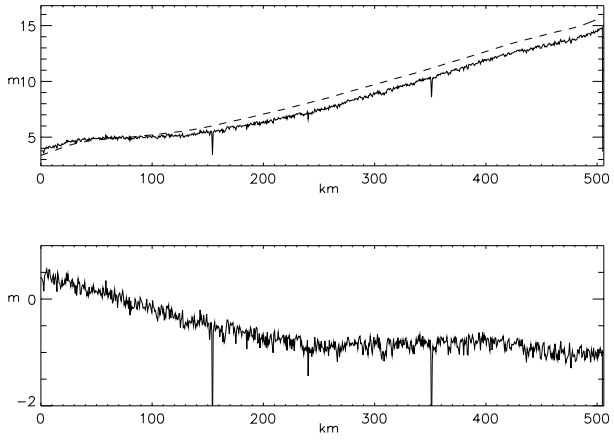

Figure C.5: Comparison of altimeter (solid) and reference geoid (dashed) derived profiles (top) and the difference between them (bottom). Differences are primarily due to long wavelength (111+ km) errors, spikes, and higher frequency features that represent both noise and crustal signals. Profile shown is ERS-1 168-day mission track 26138 and is sampled roughly every 660 meters.

first component in Equation C.1. The second term may be easily determined and added to the first to generate the desired FAGA.

Hence, reference profiles were removed from observed profiles to generate residual profiles, which were then bandpassed filtered between 4 and 111 km wavelengths to remove long wavelength errors and high frequency noise. As a first grouping, profiles are separated by mode (ascending or descending), to take advantage of the sub-parallel nature of the tracks. Analysis for profiles in both modes proceeds separately until a final residual geoid undulation map is to be generated. The residual profiles are geographically ordered by intercept longitude at a chosen latitude (usually in the middle of the study area), thereby placing profiles in order from West to East for ease of comparison.

Adjacent track pairs are then interpolated into a power of two and Fourier transformed into the wavenumber domain. The individual wavenumber components between each pair of neighboring tracks are correlated based upon their phase difference. Small phase differences imply wavenumber components that are strongly correlated and which may be derived from the same geologic features. The cosine of the phase difference gives the coefficient of correlation (CC) of each wavenumber pair. The effect on the overall power of selectively removing those wavenumbers that have progressively higher correlations is plotted (Figure C.6) and a critical cutoff point is established where the power drop off of the passed wavenumber components becomes very steep. This cutoff CC (CCk) is used to pass maximum power while removing those wavenumbers that correlate the least. The elimination of these wavenumbers occurs independently depending on whether they correlate better or worse than the cutoff CC (notch filtering). The remaining wavenumbers are then inversely transformed to reconstruct the track pair. The two profiles are averaged to produce a least squares estimate of the common signals and assigned to the median locations of the original two profiles.

These averaged profiles then most nearly represent residual geoid undulation profiles for an ascending or descending direction. To remove directional effects a quadrant swapping method [Kim, 1993; Kim et al., 1998] is utilized instead of a crossover adjustment. This method helps to reduce the corrugated effect associated with residual track line bias when gridding. The two separate data modes are gridded and inversely transformed to generate Fourier spectra, where the effects of the individual track directions are apparent as a band in the quadrants orthogonal to the mode directions (eg., a band would appear in the upper-left and lower-right quadrants of the amplitude spectrum for descending data, which would pass through the upper-right and lower-left quadrants in the data domain). By retaining the two relatively

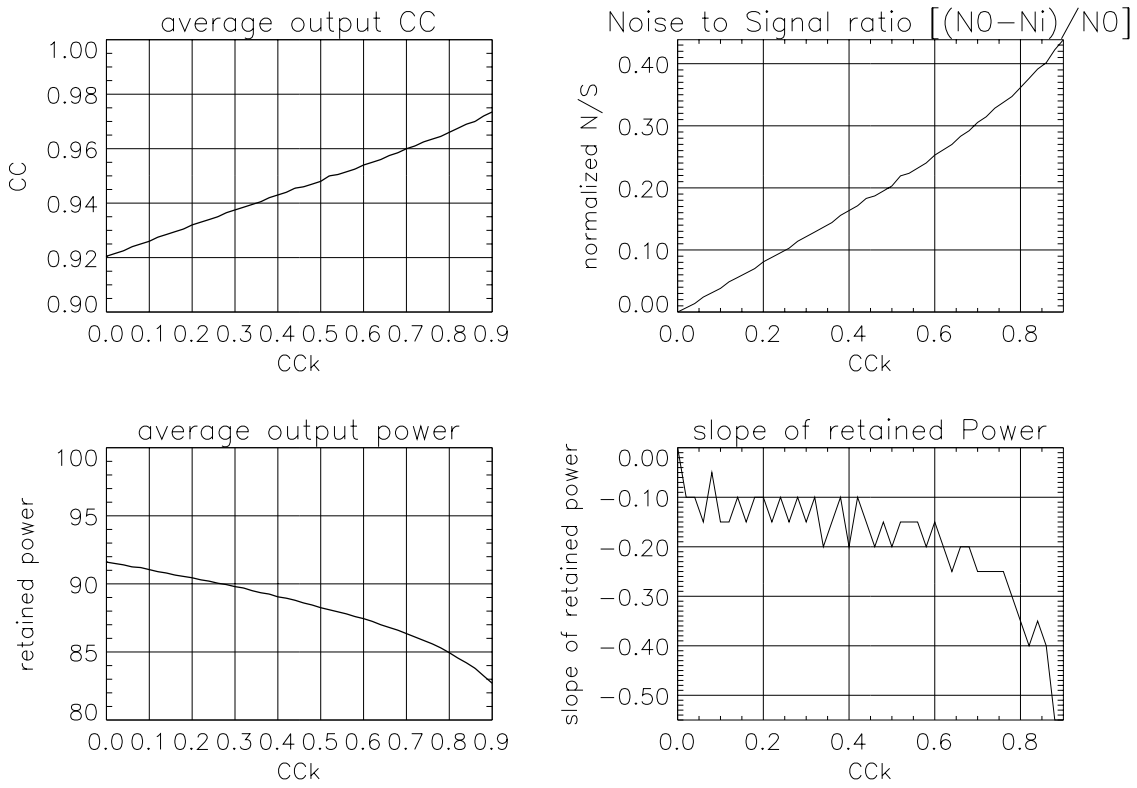

Figure C.6: Power spectrum and trade-off diagram showing cutoff correlation (CCk) selection. Increase in overall track pair correlations and improvement in signal to noise ratio are nearly linear (upper-right and upper-left diagrams) and the drop off in power is nearly linear except at the highest values (bottom-left diagram). The slope of the power drop off (bottom-right diagram) more clearly shows that the maximal inflection point is at about a CC of 0.8 to 0.9. For this reason, 0.9 was chosen for the CCk).

uncontaminated quadrants from each data mode, a composite Fourier spectrum may be generated. This composite spectrum is then inversely transformed to generate a final residual geoid undulation grid (Figure C.7).

The residual geoid undulation may now be transformed into a residual FAGA grid (Figure C.8) through application of the fundamental equation of geodesy as expressed in a Fourier transform [Kim, 1993; Schwarz et al., 1990]. The data represented in (Figure C.7) are again Fourier transformed, and the first vertical derivative is taken in the wave domain. The result is inversely transformed to yield the first term in Equation C.1. The second term is easily determined in the data domain knowing the geographic latitude of the grid points.

This final residual FAGA grid represents that component of the FAGA field between the 4 and 111 km wavelengths. To generate final predictions, it is necessary to select a wavelength for merging these data with the reference KAFAGA grid. This is necessary to prevent the overlapped wavelengths from having too much power. A value of 55 km was selected as the most optimal merging wavelength based upon comparison of the radial power spectra of the residual FAGA and KAFAGA. Because both radial power spectra contained about the same energy at the 55 km wavelength, merging at this would not create obvious discontinuities in the combined spectra.

Therefore, KAFAGA were lowpass filtered KAFAGA at 55 km, and the residual FAGA were bandpass filtered between 16 and 55 km. Wavelengths between 4 and 16 km in the residual FAGA were removed based upon the amount of incoherent signal (noise) that was being generated at those wavelengths. The two filtered grids were then added together to generate the enhanced FAGA grid (Figure C.9). This final grid is strongly similar to KAFAGA (CC=0.93), because of the long wavelength features, but they can be seen to differ in the shorter wavelengths (compare the features in Figure C.9 with those in the red box portion of Figure C.3).

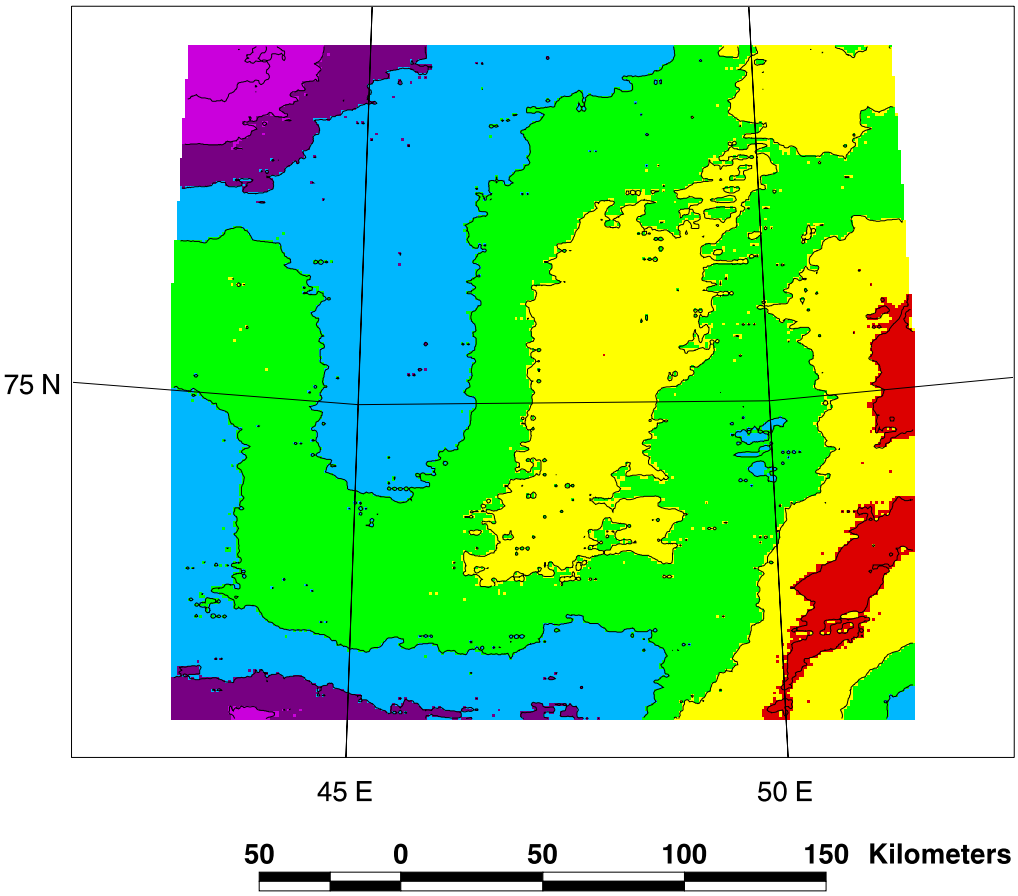

Figure C.7: Residual geoid undulation for Barents Sea test area shown in a Lambert Equal-Area Azimuthal Projection centered on 47 E at sea level.

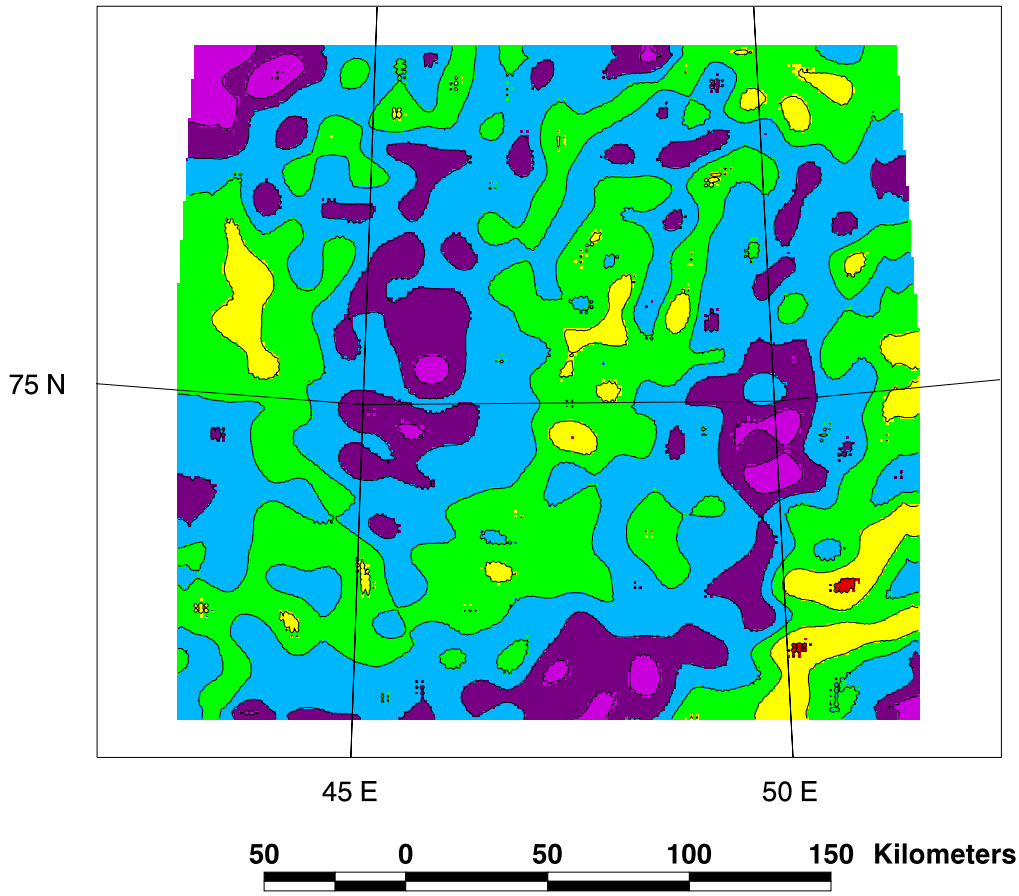

Figure C.8: Residual FAGA for Barents Sea test area shown in a Lambert Equal-Area Azimuthal Projection centered on 47 E at sea level.

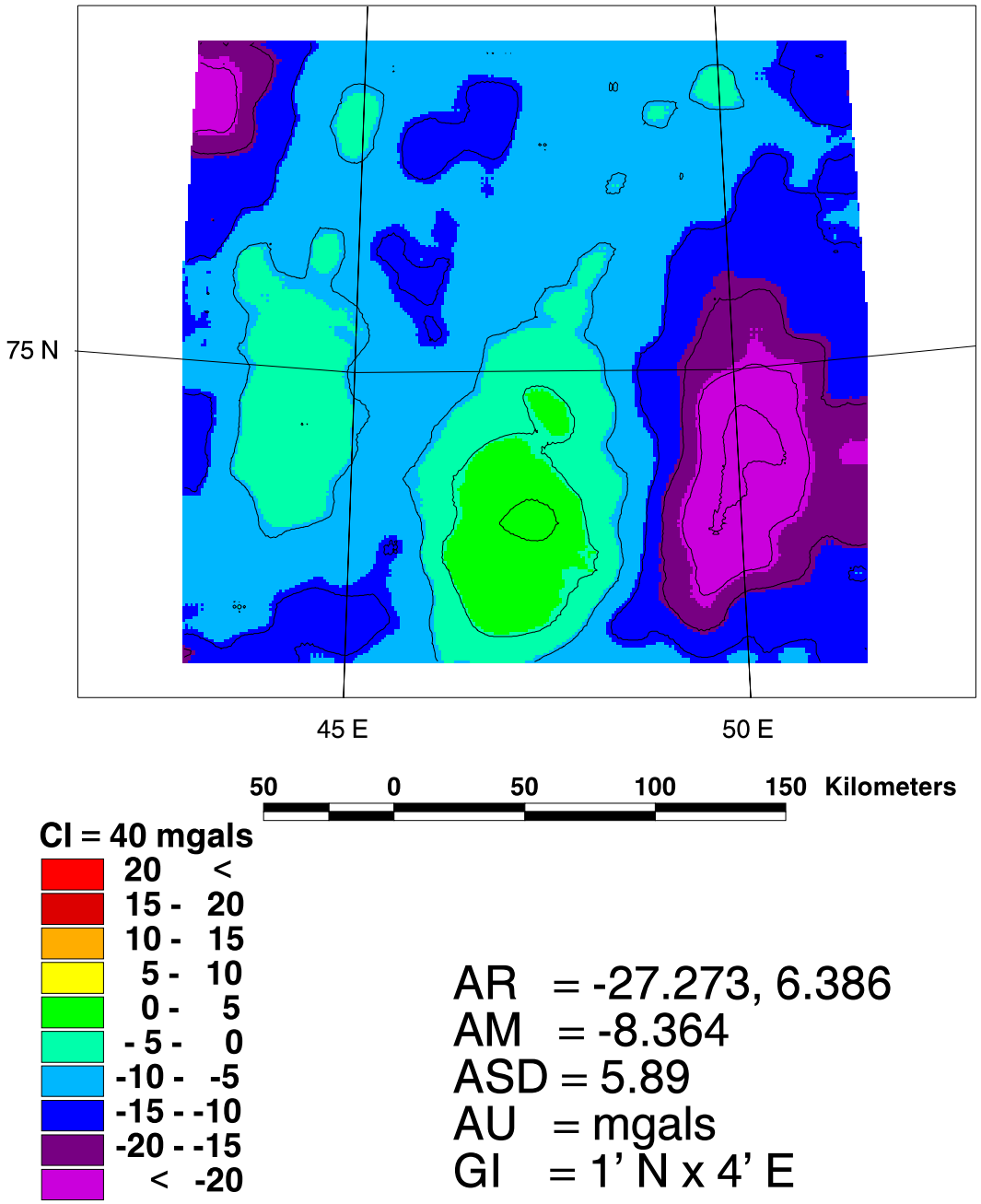

Figure C.9: Total enchanced FAGA for the Barents Sea shown in a Lambert Equal-Area Azimuthal Projection centered on 47 E at sea level. Comparison of these features to those in the red box in Figure C.3 show that the major features are still present.

Efficacy of this procedure was tested in the Gulf of Mexico [Roman, 1996], offshore of southern Africa and in the South Atlantic [Roman and von Frese, 1998a]. A reference FAGA data set derived from bottom meter and shipborne observations at about a 2 km resolution was available for comparison to the enhanced FAGA for the Gulf of Mexico region. The enhanced FAGA data showed a coherence of 50% with this reference FAGA down to the 50 km wavelength. FAGA data derived by Sandwell and Smith [1997] show agreement to the same level. Averaging the enhanced FAGA with the Sandwell and Smith FAGA diminished irregularities derived from differences in processing and lowered the 50% coherence down to the 35 km, which is about the optimum expected for Geosat data in this region [Yale et al., 1995] based upon the groundtrack coverage.

This would seem to substantiate this approach for the Gulf of Mexico region. Similar reference FAGA data sets were not available for the other two regions, however, the agreement between the enhanced FAGA and the Sandwell and Smith FAGA for these two regions was comparable to that found for the Gulf of Mexico region.

C.4 Summary

A technique for enhancing available free-air gravity anomaly (FAGA) data sets was discussed. The enhancements retain the shortest wavelengths of the Geosat altimetry to refine the shortest wavelengths (10-55 km) of the Earth's gravity field. The intermediate and longer wavelengths (55+ km) remain the same as in the selected reference FAGA data set. This retains the long wavelength character of the reference data, which should be adequately described by all the combined data. The enhanced shorter wavelengths are derived by extracting the most correlative static components of geographically adjacent altimeter profiles. These components are assumed to derive from common geologic sources in both altimeter profiles. These value-added short

wavelengths are then added back to the longer wavelengths of the reference FAGA to generate enhanced FAGA.

The resulting enhanced FAGA data are comparable to those of Sandwell and Smith [1997], which have been low pass filtered at 20 km. Merging of the enhanced and Sandwell and Smith FAGA minimizes errors in both approaches and enhances the data. This is evidenced by the further improvement in the merged data's correlation with control data in the Gulf of Mexico - to a level estimated to be the theoretical limit of quality based upon Geosat's geographic coverage.

APPENDIX D

Tabular control data for Greenland

The following data in Tables D.1 and D.2 were used to estimate the accuracies of the 3D models.

point		location		absolute	ell.	ice	FAGA	orth.
id.	station	latitude	longitude	gravity	elev.	thick.	Δg	elev.
num.	name	(deg. N)	(deg. E)	(mgals)	(m)	(m)	(mgals)	(m)
95055	wp01	77.18044	298.87903	982419.5	1906.8	-999.0	45.7	1882.0
95057	gits	77.13975	298.96100	982420.6	1897.8	-999.0	45.7	1873.0
95056	wp02	77.02370	299.93195	982416.6	1854.7	-999.0	32.9	1829.9
95058	wp03	76.88794	300.64227	982434.9	1757.0	-999.0	26.4	1732.3
95059	wp04	76.67939	301.75748	982445.1	1677.2	-999.0	20.5	1652.3
96119	wp05	76.50394	302.63733	982432.4	1637.5	-999.0	2.7	1612.3
96120	wp06	76.32359	303.48199	982413.6	1668.5	-999.0	1.0	1642.8
95049	wp07	76.14239	304.31516	982396.1	1782.5	-999.0	26.2	1755.8
95054	wp08	75.95753	305.12424	982372.7	1904.1	-999.0	48.2	1876.2
95050	wp09	75.77031	305.91260	982351.4	1945.9	-999.0	47.9	1917.0
95051	wp10	75.49508	306.52286	982335.2	1929.8	-999.0	38.8	1900.7
95052	wp12	75.27437	307.04007	982299.4	1987.0	-999.0	30.4	1957.6
95053	wp13	75.01611	307.24557	982306.4	1951.4	-999.0	38.0	1921.7
95048	wp14	74.70022	307.42026	982300.3	1888.9	-999.0	27.2	1858.7
95047	wp15	74.43411	307.54504	982302.8	1897.1	-999.0	44.6	1866.6
95046	wp16	74.16847	307.67041	982285.4	1888.6	-999.0	37.1	1858.0
95044	wp17	73.90125	307.79199	982286.7	1859.5	-999.0	42.2	1828.7
95043	wp18	73.63445	307.91098	982273.8	1838.8	-999.0	36.0	1807.8
95042	wp19	73.43300	307.99582	982256.4	1828.9	-999.0	25.4	1797.7
95041	wp20	73.19886	308.45438	982242.6	1881.0	-999.0	39.5	1849.0
95040	wp21	72.96333	308.89990	982209.9	1974.6	-999.0	47.6	1941.3
95039	wp22	72.72717	309.33380	982177.7	2075.6	-999.0	58.6	2040.9
95038	wp23	72.49008	309.75842	982134.3	2178.9	-999.0	59.4	2143.1
95037	wp24	72.25228	310.16968	982128.3	2224.3	-999.0	79.9	2187.9
95036	wp25	72.01314	310.57001	982145.4	2023.8	-999.0	47.8	1987.4
95035	wp26	71.77248	310.96066	982133.6	2029.7	-999.0	50.8	1993.5
95034	wp27	71.53267	311.34229	982093.9	2111.0	-999.0	49.1	2074.9
95033	wp28	71.29095	311.71234	982086.1	2102.2	-999.0	51.9	2065.9
95032	wp29	71.04875	312.07367	982066.7	2098.9	-999.0	44.9	2062.2
95031	wp30	70.80669	312.42819	982041.2	2097.4	-999.0	32.5	2060.4
95030	wp31	70.56281	312.77301	982028.7	2112.5	-999.0	38.5	2075.2
95029	wp32	70.31861	313.10965	982011.3	2119.5	-999.0	37.2	2081.7
95025	cd-21	69.68202	313.06625	982019.2	1909.8	-999.0	17.6	1872.7
95026	cd-38	69.52214	313.10162	982030.0	1893.4	-999.0	32.9	1856.4
95027	cd-64	69.27756	313.14642	982027.5	1828.6	-999.0	25.0	1791.6

Continued

Table D.1: BPRC-derived location, gravity and ice thickness data in Greenland. Free-air gravity anomalies were derived by differencing the absolute gravity value with a normal gravity value free-air corrected to the observation elevation. A value of -999.0 in the radar ice thickness column indicates a null value for that location.

Table D.1: Continued

point		location		absolute	ell.	ice	FAGA	orth.
id.	station	latitude	longitude	gravity	elev.	thick.	Δg	elev.
num.	name	(deg. N)	(deg. E)	(mgals)	(m)	(m)	(mgals)	(m)
95028	cd-107	68.87097	313.20636	982013.3	1808.8	-999.0	29.3	1771.4
95019	c136	68.59683	313.24966	981971.8	1826.1	-999.0	10.0	1788.2
95020	c159	68.37881	313.29138	981945.6	1873.1	-999.0	11.8	1834.8
95021	c182	68.16103	313.35971	981944.7	1875.7	-999.0	25.2	1836.7
95022	c206	67.93581	313.43048	981923.4	1923.2	-999.0	32.8	1883.2
95023	c231	67.70025	313.48917	981913.3	1955.8	-999.0	47.8	1914.8
95024	c250	67.51965	313.49341	981906.1	1972.1	-999.0	57.1	1930.4
96001	f2	67.43945	313.31592	981913.6	1936.0	-999.0	58.6	1894.4
96002	f3	67.18000	313.13916	981911.0	1914.0	-999.0	66.1	1872.0
96003	f4	66.91888	312.97006	981900.4	1882.0	-999.0	62.6	1839.9
96004	f5	66.65833	312.80334	981879.8	1898.0	-999.0	64.1	1856.1
96005	f6	66.39735	312.63971	981847.8	1922.8	-999.0	57.0	1881.3
96006	f7	66.13618	312.47839	981819.8	1932.1	-999.0	49.4	1890.8
96007	f8	65.87498	312.32336	981792.0	1927.6	-999.0	37.8	1886.6
96008	f9	65.61368	312.16986	981780.9	1919.9	-999.0	42.1	1879.2
96009	f10	65.35204	312.01910	981769.1	1943.9	-999.0	55.6	1903.4
96010	f11	65.08971	311.87103	981739.6	1944.8	-999.0	44.6	1904.3
96011	f12	64.82775	311.72742	981752.6	1888.3	-999.0	58.4	1848.0
96012	f13	64.56610	311.58554	981762.9	1831.3	-999.0	69.3	1791.6
96013	f14	64.29765	311.56506	981746.1	1784.4	-999.0	57.1	1745.0
96014	f15	64.02806	311.54568	981675.8	1876.4	-999.0	34.4	1837.3
96015	f16	63.75964	311.52640	981669.0	1903.0	-999.0	55.0	1863.9
96016	f17	63.49043	311.50735	981670.3	1894.9	-999.0	73.2	1855.6
96017	f18	63.22149	311.48941	981574.9	1912.0	-999.0	2.7	1872.3
96018	f19	62.95289	311.47156	981660.1	1911.8	-999.0	107.6	1871.9
96019	f20	62.72915	311.80081	981626.9	1952.0	-999.0	103.2	1911.0
96020	f21	62.50461	312.12436	981594.2	1855.2	-999.0	57.2	1814.0
96021	f22	62.28048	312.43985	981579.4	1832.4	-999.0	52.1	1791.3
96022	f23	62.05419	312.75473	981645.9	1900.5	-999.0	156.6	1858.9
96023	f24	61.82769	313.06296	981618.1	1954.2	-999.0	162.5	1911.9
96024	f25	61.81112	313.63046	981619.8	2123.0	-999.0	217.6	2078.8
96025	f26	61.79196	314.19711	981581.9	2220.8	-999.0	211.2	2175.2
96027	f28	61.74627	315.32690	981588.0	2184.8	-999.0	209.7	2136.4
96028	f29	61.72227	315.89523	981597.5	2091.6	-999.0	192.2	2042.5
96029	f30	61.93361	316.24533	981617.2	2172.7	-999.0	221.0	2123.2
96030	f31	62.20261	316.25781	981614.1	2160.5	-999.0	194.0	2110.5
96031	f32	62.47179	316.27090	981560.2	2122.9	-999.0	108.3	2072.9
96032	f33	62.74995	315.86636	981612.3	2465.2	-999.0	245.4	2414.2
96033	f34	63.03033	316.12515	981596.3	2392.8	800.0	186.5	2341.6
96034	f35	63.24503	316.32718	981599.2	2535.7	1005.0	217.8	2484.2

Continued

Table D.1: Continued

point		location		absolute	ell.	ice	FAGA	orth.
id.	station	latitude	longitude	gravity	elev.	thick.	Δg	elev.
num.	name	(deg. N)	(deg. E)	(mgals)	(m)	(m)	(mgals)	(m)
96035	f36	63.49422	316.56540	981609.0	2563.0	1110.0	217.9	2511.2
96036	f37	63.73913	316.80472	981616.6	2628.6	1206.0	228.1	2576.9
96037	f38	63.98901	317.04977	981560.3	2477.2	1204.0	107.1	2426.0
96038	f39	64.23389	317.30005	981620.9	2359.8	987.0	113.9	2309.1
96039	f40	64.47779	317.55508	981677.1	2072.6	1099.0	64.3	2022.6
96040	f41	64.74725	317.58133	981650.7	2203.8	1591.0	59.4	2154.1
96041	f42	65.01582	317.60895	981712.5	2119.1	1367.0	76.3	2069.7
96042	f43	65.28552	317.63864	981730.8	2003.5	1628.0	40.2	1954.4
96043	f44	65.55267	317.66553	981745.7	2035.0	1667.0	46.6	1986.1
96044	f45	65.78459	318.00610	981763.9	2035.6	1622.0	49.1	1987.0
96045	f46	66.01218	318.34552	981754.0	2101.8	1824.0	44.2	2053.3
96046	f47	66.24221	318.70358	981756.8	2129.8	1762.0	40.2	2081.1
96047	f48	66.46911	319.05737	981765.9	2209.4	-999.0	58.8	2160.3
96048	f49	66.69603	319.41699	981771.7	2194.7	-999.0	45.0	2145.3
96049	f50	66.92274	319.78754	981772.8	2186.7	-999.0	28.8	2137.2
96050	f51	67.14787	320.16406	981764.6	2269.7	-999.0	31.5	2220.0
96051	f52	67.31219	320.71738	981747.0	2348.9	-999.0	27.7	2298.5
96052	f53	67.47318	321.27255	981709.5	2482.6	-999.0	21.1	2431.0
96053	f54	67.63355	321.83942	981706.8	2628.9	-999.0	53.2	2576.0
96054	f55	67.79007	322.41507	981668.2	2754.9	-999.0	43.6	2700.7
96055	f56	67.94671	322.99634	981656.0	2886.4	2096.0	62.0	2831.2
96056	f57	68.09963	323.58398	981665.0	2977.9	1654.0	89.6	2921.8
96057	f58	68.25179	324.18500	981701.0	2931.8	1406.0	101.8	2875.2
96058	f59	68.53062	324.25504	981691.3	2799.4	2300.0	33.9	2743.4
96059	f60	68.81191	324.33093	981761.6	2753.9	1729.0	72.9	2698.4
96060	f61	69.09526	324.41483	981780.4	2696.2	1900.0	56.6	2640.9
96061	f62	69.37518	324.49200	981820.9	2720.5	1989.0	87.8	2665.1
96062	f63	69.52222	325.17978	981846.6	2720.3	1463.0	104.7	2664.2
96063	f64	69.66646	325.87146	981862.5	2664.4	1335.0	94.8	2608.2
96064	f65	69.80849	326.57544	981820.7	2696.0	1700.0	54.3	2639.5
96065	f66	69.94885	327.29025	981812.6	2769.4	1800.0	60.6	2712.3
96066	f67	70.22163	327.38062	981798.6	2871.5	2077.0	62.2	2814.7
96067	f68	70.49577	327.47382	981828.1	2870.0	1914.0	75.6	2813.9
96068	f69	70.76944	327.56656	981845.7	2816.3	2001.0	61.0	2761.3
96069	f70	71.04166	327.66376	981859.6	2785.3	2205.0	50.1	2731.3
96070	f71	71.31603	327.76578	981897.3	2747.7	2092.0	60.9	2694.3
96071	f72	71.58830	327.86819	981912.3	2701.8	2153.0	46.8	2649.0
96073	f75	72.13501	328.08469	981891.5	2749.5	2416.0	11.4	2698.2
96072	f74	72.40752	328.19888	981948.3	2855.6	1500.0	86.6	2804.9
96074	f76	72.67838	328.32465	981915.9	2903.6	1615.0	54.9	2853.2

Continued

Table D.1: Continued

point		location		absolute	ell.	ice	FAGA	orth.
id.	station	latitude	longitude	gravity	elev.	thick.	Δg	elev.
num.	name	(deg. N)	(deg. E)	(mgals)	(m)	(m)	(mgals)	(m)
96075	f77	72.95300	328.43372	981932.0	2912.2	1747.0	59.5	2861.9
96076	f78	73.22584	328.55673	981947.5	2916.8	1348.0	62.7	2866.8
96077	f81	73.50395	328.69742	981981.2	2890.1	823.0	74.2	2840.7
96078	f82	73.77976	328.93805	982020.5	2821.1	686.0	78.7	2772.4
96079	f83	74.05439	329.18698	982006.9	2773.6	955.0	37.2	2725.5
96080	f84	74.32832	329.45142	982063.0	2729.3	1442.0	66.6	2681.8
96081	f85	74.60120	329.73035	982096.1	2655.5	1357.0	64.1	2608.7
96082	f86	74.87357	330.01639	982087.8	2663.3	1796.0	45.6	2617.0
96083	f87	75.14738	330.30682	982097.2	2585.5	2085.0	18.6	2539.3
96084	f88	75.41988	330.61261	982183.0	2536.9	1648.0	77.2	2490.1
96085	f89	75.69181	330.92831	982226.0	2462.8	2022.0	85.4	2415.3
96086	f90	75.96321	331.25735	982290.7	2365.0	1376.0	108.2	2317.2
96087	f91	76.23466	331.60245	982326.8	2287.8	1428.0	109.0	2240.4
96088	f92	76.50513	331.95523	982402.9	2178.0	831.0	139.9	2131.7
96089	f96	76.77868	332.32922	982412.7	2049.0	1530.0	98.8	2004.2
96090	f97	77.02991	331.89987	982442.3	1912.1	1457.0	76.1	1868.7
96091	f98	77.28230	331.49570	982456.6	1854.1	1705.0	62.6	1812.0
96092	f99	77.53101	331.02560	982484.3	1817.3	1440.0	69.2	1776.2
96093	f100	77.77999	330.55496	982498.9	1759.1	1523.0	56.4	1718.8
96094	f101	78.02887	330.06564	982522.4	1729.2	1387.0	61.4	1689.8
96095	f102	78.32616	329.44821	982504.8	1758.6	1674.0	42.1	1720.1
96096	f103	78.62091	328.80927	982517.8	1768.7	1565.0	47.7	1730.7
96097	f104	78.91445	328.13513	982522.5	1800.1	1585.0	51.9	1762.5
96098	f105	79.20844	327.41010	982518.4	1832.6	1673.0	47.9	1795.2
96099	f106	79.49748	326.66086	982518.5	1889.8	1766.0	56.1	1852.1
96100	f107	79.78625	325.86435	982531.9	1941.6	1769.0	76.2	1903.7
96101	f108	80.07324	325.02707	982528.7	1956.2	1792.0	68.5	1918.9
96102	f109	80.35745	324.13358	982521.7	1914.6	1631.0	40.1	1878.3
96103	f110	80.63997	323.18909	982544.4	1871.8	1719.0	41.1	1836.1
96104	f113	80.91976	322.17819	982597.2	1847.6	1322.0	78.4	1812.3
96105	f114	80.75153	320.08655	982516.2	2008.5	1749.0	51.9	1973.9
96106	f115	80.57153	318.06104	982494.7	2035.1	1711.0	43.9	2001.7
96107	f116	80.38071	316.10248	982485.8	2033.1	1709.0	40.1	2000.7
96108	f117	80.17941	314.23758	982485.1	2032.3	1823.0	45.2	2001.0
96109	f118	79.96825	312.44284	982466.2	2028.6	1963.0	31.6	1998.3
96110	f119	79.74799	310.72461	982443.7	2021.2	2376.0	13.8	1991.4
96111	f120	79.51905	309.07764	982475.4	1963.7	1860.0	35.1	1934.3
96112	f121	79.28233	307.50296	982466.1	1959.8	1967.0	32.4	1931.1
96113	f122	79.03761	305.99194	982452.0	1968.1	2035.0	29.1	1939.9
96114	f123	78.78490	304.55078	982448.0	1981.5	1945.0	37.9	1953.4
96115	fh01	78.25407	302.24460	982435.9	2028.8	1894.0	59.1	2000.3
96116	fh02	77.97932	301.37094	982439.2	2074.9	1709.0	86.8	2046.7
96117	fh03	77.70087	300.52982	982393.4	2082.1	1949.0	53.6	2055.0
96118	fh04	77.41975	299.72412	982381.8	2011.6	1800.0	31.0	1985.9

point	Ekholm			NIMA	
id. no.	ice surface (m)	ice bottom (m)	ice thickness (m)	ice surface (m)	FAGA (mgals)
95055	1877.8	564.4	1313.4	1875.2	31.5
95057	1870.0	555.0	1315.0	1869.5	32.3
95056	1819.4	384.5	1434.9	1814.5	19.4
95058	1745.5	330.1	1415.4	1741.2	19.3
95059	1662.5	316.7	1345.8	1661.8	11.3
96119	1627.4	184.9	1442.5	1624.5	-12.9
96120	1686.0	305.5	1380.5	1675.6	-7.0
95049	1740.1	450.0	1290.1	1746.5	16.8
95054	1854.9	593.4	1261.5	1850.7	38.7
95050	1914.7	506.9	1407.8	1910.8	36.2
95051	1915.0	454.1	1460.9	1909.5	22.6
95052	1941.8	418.9	1522.9	1937.3	10.1
95053	1915.2	511.0	1404.2	1911.1	22.1
95048	1872.1	452.9	1419.2	1871.3	26.3
95047	1863.1	437.1	1426.0	1859.6	28.9
95046	1851.1	385.7	1465.4	1850.3	26.0
95044	1832.9	419.8	1413.1	1829.2	27.9
95043	1803.1	412.2	1390.9	1800.1	16.9
95042	1789.9	398.5	1391.4	1784.4	18.4
95041	1847.5	480.4	1367.1	1846.5	24.1
95040	1941.8	603.8	1338.0	1942.7	18.7
95039	2046.9	695.2	1351.7	2040.2	43.0
95038	2144.0	759.3	1384.7	2141.9	44.6
95037	2183.0	897.0	1286.0	2175.3	64.8
95036	1987.4	717.8	1269.6	1980.1	36.9
95035	1977.1	702.6	1274.5	1972.7	44.6
95034	2073.2	601.1	1472.1	2071.1	37.2
95033	2067.3	313.9	1753.4	2064.1	19.1
95032	2055.1	251.4	1803.7	2052.4	27.4
95031	2060.7	242.9	1817.8	2058.5	23.1
95030	2070.9	217.4	1853.5	2067.0	19.3
95029	2075.0	167.0	1908.0	2073.3	28.2
95025	1891.4	-4.9	1896.3	1901.7	12.5
95026	1855.0	16.5	1838.5	1851.1	12.4
95027	1794.7	30.3	1764.4	1805.4	20.6
95028	1769.3	22.4	1746.9	1768.0	9.9

Continued

Table D.2: Height, thickness and FAGA data interpolated from 3D data for the BPRC data points on Greenland.

Table D.2: Continued

point id. no.	Ekholm			NIMA	
	ice surface (m)	ice bottom (m)	ice thickness (m)	ice surface (m)	FAGA (mgals)
95019	1787.0	-152.0	1939.0	1796.1	-6.0
95020	1833.0	-112.9	1945.9	1827.4	-6.4
95021	1836.6	6.8	1829.8	1832.3	8.4
95022	1883.3	115.4	1767.9	1879.0	23.8
95023	1911.7	187.5	1724.2	1907.1	36.7
95024	1928.3	242.6	1685.7	1927.3	42.9
96001	1894.2	289.3	1604.9	1894.0	44.1
96002	1876.7	398.3	1478.4	1874.7	60.6
96003	1837.3	440.8	1396.5	1836.5	61.4
96004	1848.7	513.2	1335.5	1844.6	37.4
96005	1891.4	573.4	1318.0	1892.8	37.0
96006	1886.5	519.9	1366.6	1885.3	50.2
96007	1874.1	549.2	1324.9	1873.8	30.2
96008	1874.0	585.8	1288.2	1871.6	59.7
96009	1897.8	658.6	1239.2	1890.1	41.4
96010	1896.2	809.4	1086.8	1899.8	51.3
96011	1860.5	950.2	910.3	1856.2	55.8
96012	1792.1	949.2	842.9	1793.1	57.7
96013	1775.0	879.3	895.7	1766.9	37.2
96014	1810.2	854.2	956.0	1790.4	39.2
96015	1842.5	1146.3	696.2	1842.0	43.0
96016	1884.3	1460.6	423.7	1866.9	58.3
96017	1905.2	1623.6	281.6	1894.4	27.3
96018	1853.2	1567.5	285.7	1841.2	67.9
96019	1904.1	1432.4	471.7	1887.3	79.6
96020	1813.6	1278.3	535.3	1807.6	60.3
96021	1804.1	1278.8	525.3	1799.3	42.3
96022	1871.8	1433.8	438.0	1865.5	46.3
96023	1914.6	1645.7	268.9	1898.4	63.4
96024	2069.1	1707.7	361.4	2060.3	91.2
96025	2101.6	1667.6	434.0	2090.7	115.0
96027	2136.8	1421.2	715.6	2142.9	84.0
96028	2198.2	1479.5	718.7	2189.7	76.0
96029	2154.4	1349.7	804.7	2101.6	102.6
96030	2155.2	1244.3	910.9	2151.1	92.9
96031	2117.0	1482.2	634.8	2134.4	94.3
96032	2418.5	1390.8	1027.7	2425.8	94.1
96033	2386.2	1460.2	926.0	2373.3	132.2
96034	2478.9	1267.5	1211.4	2449.3	96.4
96035	2511.1	1235.2	1275.9	2508.0	91.2

Continued

Table D.2: Continued

point id. no.	Ekholm			NIMA	
	ice surface (m)	ice bottom (m)	ice thickness (m)	ice surface (m)	FAGA (mgals)
96036	2567.1	1300.1	1267.0	2563.9	105.3
96037	2431.4	1250.5	1180.9	2439.1	81.0
96038	2304.6	1331.1	973.5	2311.1	96.4
96039	2020.2	1009.6	1010.6	2026.8	57.1
96040	2146.1	1042.1	1104.0	2148.5	52.5
96041	2086.3	956.5	1129.8	2084.8	68.2
96042	1952.2	533.6	1418.6	1953.3	64.0
96043	1981.7	368.0	1613.7	1981.1	39.6
96044	1988.6	341.6	1647.0	1991.6	27.3
96045	2042.3	346.1	1696.2	2042.6	25.5
96046	2090.9	371.9	1719.0	2091.5	22.7
96047	2153.2	343.5	1809.7	2152.0	41.5
96048	2146.4	186.3	1960.1	2148.9	20.8
96049	2146.2	157.4	1988.8	2146.1	17.7
96050	2227.5	231.3	1996.2	2233.4	17.0
96051	2306.8	298.8	2008.0	2307.8	13.0
96052	2429.7	385.7	2044.0	2425.0	17.4
96053	2572.4	526.6	2045.8	2571.7	34.6
96054	2719.3	780.2	1939.1	2718.5	51.7
96055	2829.7	965.8	1863.9	2824.1	65.2
96056	2924.6	1240.1	1684.5	2922.5	85.1
96057	2881.1	1371.6	1509.5	2874.2	82.4
96058	2736.6	895.1	1841.5	2742.8	57.9
96059	2708.1	867.7	1840.4	2707.8	54.3
96060	2646.1	980.7	1665.4	2650.0	61.9
96061	2657.1	876.4	1780.7	2660.1	82.8
96062	2666.1	967.0	1699.1	2659.7	103.6
96063	2601.5	944.6	1656.9	2610.9	69.5
96064	2646.2	890.0	1756.2	2645.0	43.0
96065	2711.1	947.7	1763.4	2706.8	54.6
96066	2811.7	946.2	1865.5	2812.3	51.9
96067	2813.2	924.2	1889.0	2814.7	53.8
96068	2762.4	745.1	2017.3	2763.9	34.1
96069	2733.5	649.7	2083.8	2733.1	29.4
96070	2689.5	670.3	2019.2	2692.4	38.7
96071	2646.2	653.0	1993.2	2646.7	35.1
96073	2800.6	868.0	1932.6	2802.2	19.8
96072	2732.3	697.5	2034.8	2736.2	20.0
96074	2851.0	1003.2	1847.8	2853.6	38.0
96075	2861.0	1137.8	1723.2	2861.0	29.2

Continued

Table D.2: Continued

point id. no.	Ekholm			NIMA	
	ice surface (m)	ice bottom (m)	ice thickness (m)	ice surface (m)	FAGA (mgals)
96076	2847.5	1309.7	1537.8	2845.9	42.1
96077	2824.2	1518.8	1305.4	2827.6	59.1
96078	2767.8	1581.7	1186.1	2769.3	63.3
96079	2725.0	1430.6	1294.4	2726.1	16.7
96080	2691.4	1366.0	1325.4	2690.6	38.7
96081	2618.7	1160.9	1457.8	2621.7	32.2
96082	2598.2	917.3	1680.9	2599.1	28.5
96083	2539.2	833.9	1705.3	2541.0	-4.8
96084	2489.5	717.6	1771.9	2490.9	45.6
96085	2416.2	737.3	1678.9	2415.4	85.3
96086	2300.2	850.3	1449.9	2303.8	93.5
96087	2241.1	839.1	1402.0	2239.3	91.1
96088	2128.9	802.7	1326.2	2132.7	110.5
96089	2001.1	699.7	1301.4	1999.9	85.7
96090	1865.9	534.6	1331.3	1869.6	79.1
96091	1816.5	407.7	1408.8	1824.0	50.0
96092	1767.2	277.8	1489.4	1769.7	38.7
96093	1719.6	137.1	1582.5	1718.4	40.5
96094	1678.8	148.1	1530.7	1681.1	44.1
96095	1707.0	226.6	1480.4	1709.8	30.4
96096	1732.5	162.9	1569.6	1730.7	26.6
96097	1764.0	230.4	1533.6	1765.4	36.0
96098	1792.2	273.9	1518.3	1791.8	25.4
96099	1855.6	211.1	1644.5	1855.9	49.2
96100	1905.0	216.4	1688.6	1905.0	61.9
96101	1920.0	179.3	1740.7	1920.0	53.1
96102	1878.9	173.5	1705.4	1879.7	32.8
96103	1834.0	317.4	1516.6	1833.4	37.3
96104	1812.5	517.2	1295.3	1816.3	65.3
96105	1973.3	559.6	1413.7	1973.6	58.4
96106	2002.2	702.7	1299.5	2001.4	39.6
96107	2001.7	672.8	1328.9	2002.1	29.3
96108	2000.0	496.1	1503.9	1998.2	23.4
96109	1999.0	342.5	1656.5	2001.5	18.3
96110	1992.7	226.1	1766.6	1993.1	16.2
96111	1942.7	161.9	1780.8	1942.6	26.2
96112	1930.9	137.9	1793.0	1930.7	22.1
96113	1941.2	113.1	1828.1	1941.6	19.7
96114	1953.8	138.7	1815.1	1953.8	27.1
96115	2004.5	115.8	1888.7	2003.7	49.1
96116	2051.9	235.9	1816.0	2053.7	75.2
96117	2059.2	229.5	1829.7	2058.3	51.0
96118	1988.0	354.7	1633.3	1985.2	24.0

APPENDIX E

Seismic Control Depths for Greenland

Abstract

A model of the depth to the Moho was derived from available free-air gravity anomaly data and digital elevation models. This grid is interpolated to the individual locations of seismically determined control depths to perform a statistical comparison to assess the quality of the grid. The 39 control depths were assumed to be without error and correlated with their gridded equivalents at 0.89, had a mean difference of 0.1 km, and had an RMS difference of $\pm$4.6 km. This RMS difference could be made dimensionless by dividing the misfit at each station by the seismic depth. The resulting percentile, representing the magnitude of the difference with respect to the seismic estimates, was 18.3% for all values. There were six problematic values that arose primarily due to deviations away from the uniform density assumptions and to possible errors in the locations of the seismic estimates. If these 6 are excluded, then the correlation is 0.95, the mean difference is 0.4 km, the RMS difference is $\pm$3.4 km, and the percentile RMS difference is 13.1%. The overall agreement indicates that the Moho model may be reliablely used to model regional effects, although local problems may arise where erroneous density assumptions were used.

E.1 Introduction

In Chapter 3, a Moho model was generated using available free-air gravity anomalies and digital elevation models for the terrain. To assess the quality of this Moho model, comparison is made to depths obtained through seismic surveys for regions in and around Greenland. No information was provided concerning the quality of these seismic depth estimates, so they will be assumed to be with out error for purposes of determining agreement. It is assumed that general agreement between Moho model derived values and seismically derived values indicates that both are correct. Disagreement indicates that one or both are incorrect, and these comparisons will be discarded.

These seismic estimates were used to generate a long wavelength depth model and to check the agreement with the final Moho model. The depth model was generated by gridding the available seismic estimates and smoothing the resulting grid to produce a long wavelength field. This field was incorporated into the early Moho model to constrain the iteration process used to generate the final Moho model. Values were interpolated from final Moho model to the locations determined for the seismic estimates. These interpolated values and the seismic estimates are then compared and differenced to determine basic statistics.

There were six separate surveys that provided seismic estimates for the depth to the Moho [Chian & Louden, 1994; Chian & Louden, 1992; Dahl-Jensen et al., 1998; Fechner & Jokat, 1996; Gregersen et al., 1988; Jackson & Reid, 1994; Reid & Jackson, 1997]. Only two of these surveys provided complete location data with the seismic estimates [Chian & Louden[1992; 1994]. For the other surveys, the location data were determined by manually interpolating their final maps to obtain estimates of

the depth locations. Due to inaccuracies in this measurement, incorrect interpolated values may occur, which would then affect the statistical comparisons.

Another source of errors may derive from the assumption that the Moho undulation is the chief source of variation in masses and not a lateral or vertical density variation. When the Moho model was calculated, a uniform density was assumed for the crustal and mantle material. This generated a fixed density contrast. This is not a completely valid assumption. To a first order, this assumption may account for the generated gravity field, but local density variations will be modeled as Moho undulations instead. Therefore, predictions in regions containing significant density variations will deviate from the actual Moho depth.

E.2 Comparison of Interpolated Moho Model and Seismic Depths

Data in Table E.1 show Moho control values (Figure E.3) derived from various literature sources and interpolated from the Moho shown in Figure E.2. Only 39 stations fall within the actual prediction area, and these fall roughly along 7 different profiles. These profiles are displayed in Figure E.1 and the data points are analyzed further in Table E.2.

From Figure E.1, several of the profiles can be seen to agree very well, while others are anti-correlative. The first profile starts over oceanic bedrock passes over transitional crust and onto continental crust [Chian and Louden, 1994]. The second profile [Chian and Louden, 1992] parallels the coast over continental crust. The third profile [Dahl-Jensen et al., 1998] is over oceanic crust offshore southeastern Greenland. The fourth profile [Fechner and Jokat, 1996] is over continental crust in the Scoresby Sund. The data from Gregersen et al. [1988] is actually a series of distant points. The sixth profile [Jackson and Reid, 1994] and the seventh profile [Reid and Jackson,

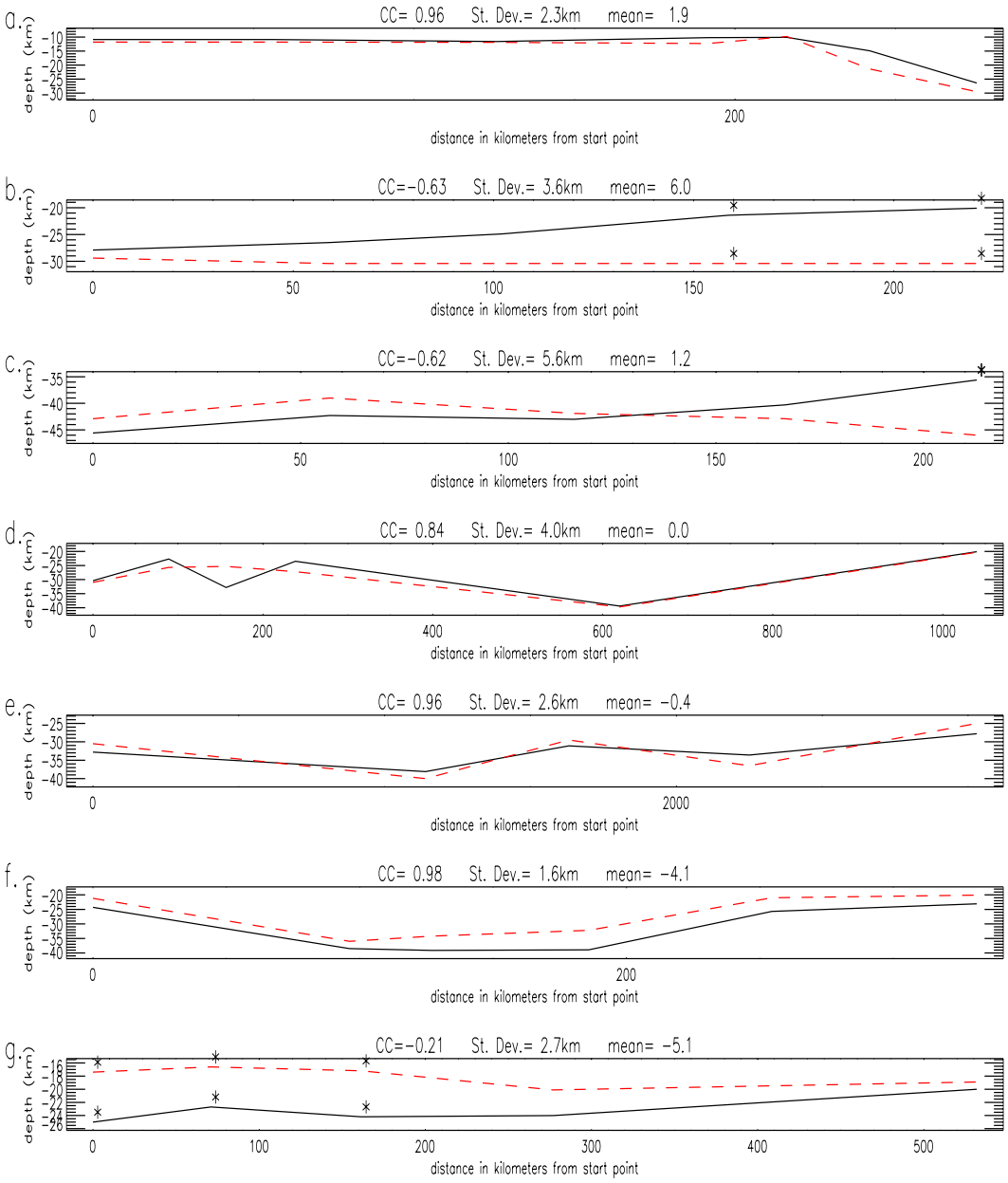

Figure E.1: Comparison of 7 seismic profiles around Greenland. Values interpolated from the final Moho model (Figure E.2) are shown as solid white profiles with the seismic estimates given in the red dashed profiles. The correlation coefficient (CC), standard deviation (St. Dev.), and mean difference (mean) are given at the top of each profile. **a.** Chian and Louden [1994] **b.** Chian and Louden [1992] **c.** Dahl-Jensen et al. [1998] **d.** Fechner and Jokat [1996] **e.** Gregersen et al. [1988] **f.** Jackson and Reid [1994] **g.** Reid and Jackson [1997]. Asterisks (*) mark points flagged for removal.

1997] are over northern Baffin Bay in a region that is partially oceanic, transitional, and continental crust.

The first, fourth, fifth, and sixth pairs of profiles show high correlation and low standard deviations between their interpolated and seismic depth estimates. The first profile covers all types of crust, the fourth and fifth are exclusively continental crust, and the sixth covers exclusively oceanic crust. Both the fifth (continental crust) and sixth (oceanic crust) have negative mean values, demonstrating that there is no dependence between crustal type and either under- or over-predicting depths.

Finally, there are six point flagged with asterisks (*) indicating points where the amount of disagreement between the interpolated and seismic values is greatest. These data are examined further in Table E.2. In Table E.2, the numeric difference between the control and predicted values are given in kilometers. These values are further divided by the seismic depth to provide percentage estimates of the magnitude of the numeric error.

If no data are removed, then the 39 points correlate at 0.89 (calculated in accordance with Davis [1986]), the numeric RMS difference was 4.6 km, the mean numeric difference was 0.1 km, and the percent RMS difference was 18.3%. Three values fell outside of the range of $\pm 2\sigma$ for the numeric differences (stations 11, 12, and 17), and three other stations (35, 36, and 37) fell outside of $\pm 2\sigma$ for the percent RMS difference.

Removing only the first group of three (denoted with a † in Table E.2) increases the CC to 0.93, reduces the numeric RMS difference to 3.7 km, increases the mean numeric difference to 0.9 km, and reduces the percent RMS difference slightly to 17.1%. Removal of the other three stations (denoted with a ‡ in Table E.2) increases the CC only to 0.91, reduces the numeric RMS difference only to 4.3 km, increases the mean numeric difference to -0.5 km, and reduces the percent RMS difference

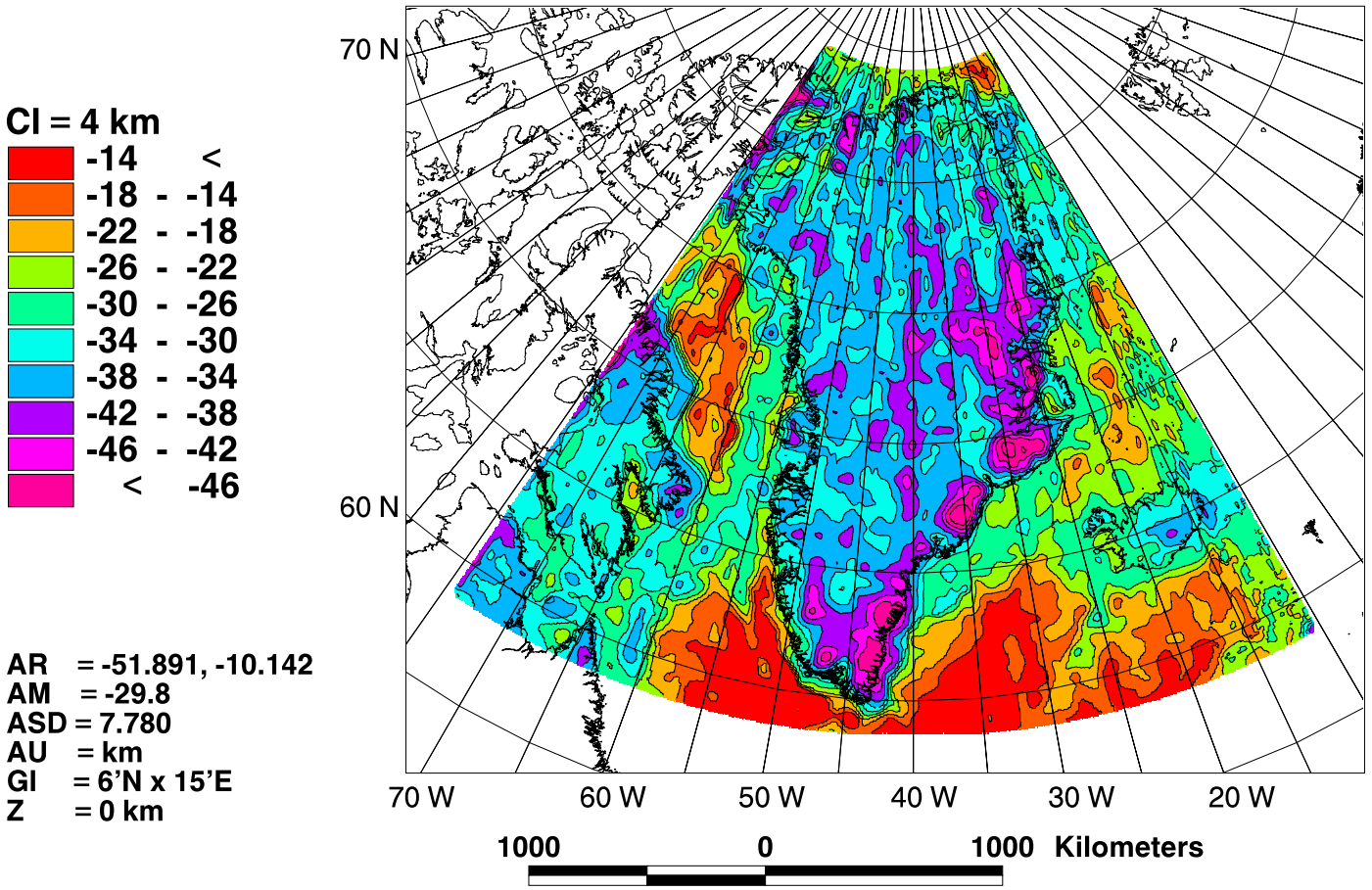

Figure E.2: Moho model for the Greenland field area shown in a Lambert Equal-Area Azimuthal Projection centered on 40 W.

Location		Moho Depth		sta.	seismic	point
latitude	longitude	seis.	mod.	id.	literature	name
(deg. N)	(deg. W)	(km)	(km)	no.	source	
59.8408	52.033	11.8	10.9	1	Chian & Louden, 1994	R2,A
60.0517	51.2900	11.8	10.9	2	Chian & Louden, 1994	R2,B
60.2767	50.4233	11.9	11.6	3	Chian & Louden, 1994	R2,C
60.4442	49.7767	12.3	10.2	4	Chian & Louden, 1994	R2,D
60.5516	49.3514	9.8	10.1	5	Chian & Louden, 1994	R2,E
60.6633	48.9100	21.4	14.9	6	Chian & Louden, 1994	R2,F
60.7400	48.6133	29.5	26.4	7	Chian & Louden, 1994	R2,G
60.5376	48.2981	29.4	27.9	8	Chian & Louden, 1992	R1,J
61.0118	49.0482	30.4	26.5	9	Chian & Louden, 1992	R1,K
61.3322	49.5552	30.4	24.9	10	Chian & Louden, 1992	R1,L
61.5943	49.9990	30.4	21.4	11	Chian & Louden, 1992	R1,M
61.8845	50.4750	30.4	20.1	12	Chian & Louden, 1992	R1,N
60.7542	42.4839	42.9	45.6	13	Dahl-Jensen et al., 1998	50km
61.1960	42.2179	39.0	42.3	14	Dahl-Jensen et al., 1998	100km
61.6007	41.7633	41.9	43.0	15	Dahl-Jensen et al., 1998	150km
62.0555	41.6283	42.9	40.3	16	Dahl-Jensen et al., 1998	200km
62.4576	41.1833	46.0	35.6	17	Dahl-Jensen et al., 1998	250km
70.7689	25.2885	31.0	30.4	18	Fechner & Jokat, 1996	90544 W
70.8297	24.2372	25.7	22.7	19	Fechner & Jokat, 1996	90544 E
70.2230	24.2964	25.3	32.8	20	Fechner & Jokat, 1996	90539 S
70.9568	24.4240	27.2	23.5	21	Fechner & Jokat, 1996	90539 N
70.3933	27.8433	39.7	39.4	22	Fechner & Jokat, 1996	90320 W
70.6289	24.0444	20.3	20.1	23	Fechner & Jokat, 1996	90320 E
69.2254	53.5769	30.5	32.8	24	Gregersen et al., 1988	GDH
77.6812	38.6207	40.0	38.1	25	Gregersen et al., 1988	ILG
81.7101	15.9596	29.5	31.1	26	Gregersen et al., 1988	NOR
76.5507	18.3951	36.5	33.6	27	Gregersen et al., 1988	DAG
70.2778	21.6667	25.0	27.8	28	Gregersen et al., 1988	KTG

Continued

Table E.1: Seismic control depths for the Greenland Moho model derived from seismic survey literature. Listed are the positional coordinates, seismic depth in kilometers, depth in kilometers interpolated from the Moho model, the seismic literature source, and the literature sources' seismic survey line and point names associated with the seismic depth values. A dash (-) in the interpolated Moho depth column indicates that the source was outside of the region covered by the Moho grid. The 39 stations that have depth values are numerically identified below (stat. id. no.) and map to the values that are analyzed in Table E.2.

Table E.1: Continued

Location		Moho Depth		sta.	seismic	point
latitude	longitude	seis.	mod.	id.	literature	name
(deg. N)	(deg. W)	(km)	(km)	no.	source	
75.0704	78.1818	27.6	-		Jackson & Reid, 1994	1,B
75.3842	77.4545	27.6	-		Jackson & Reid, 1994	1,E
75.6334	76.9143	27.4	-		Jackson & Reid, 1994	1,I
76.2676	75.1961	21.3	-		Jackson & Reid, 1994	1,J
76.5070	74.5000	21.3	-		Jackson & Reid, 1994	1,L
76.7512	73.8200	21.2	24.3	29	Jackson & Reid, 1994	1,S
77.4225	73.2414	36.0	38.5	30	Jackson & Reid, 1994	3,A
77.1455	72.6122	34.2	39.1	31	Jackson & Reid, 1994	3,C
76.7465	71.9394	32.2	38.9	32	Jackson & Reid, 1994	3,F
76.3052	71.0600	21.0	25.7	33	Jackson & Reid, 1994	3,G
75.7625	70.2991	20.1	23.1	34	Jackson & Reid, 1994	3,N
76.1282	76.7158	21.0	-		Reid & Jackson, 1997	2,R
76.1538	75.6211	21.0	-		Reid & Jackson, 1997	2,S
76.1540	75.1111	20.6	-		Reid & Jackson, 1997	2,E
76.1564	74.3263	19.3	-		Reid & Jackson, 1997	2,B
76.1590	73.8974	17.4	25.0	35	Reid & Jackson, 1997	2,I
76.1615	73.2579	16.6	22.7	36	Reid & Jackson, 1997	2,J
76.1704	72.4000	17.2	24.2	37	Reid & Jackson, 1997	2,L
76.1790	70.8842	20.1	24.0	38	Reid & Jackson, 1997	2,D
75.2051	77.9158	28.0	-		Reid & Jackson, 1997	4,S
75.1795	77.6040	25.4	-		Reid & Jackson, 1997	4,R
75.0154	77.1165	21.3	-		Reid & Jackson, 1997	4,J
74.8974	76.5857	19.2	-		Reid & Jackson, 1997	4,E
74.6819	76.0952	19.0	-		Reid & Jackson, 1997	4,D
74.4148	75.1650	19.0	-		Reid & Jackson, 1997	4,I
74.1959	74.5146	19.0	-		Reid & Jackson, 1997	4,B
73.9949	73.8095	18.9	20.0	39	Reid & Jackson, 1997	4,L

station	DEPTHS		DIFFERENCES		
id no.	predicted	control	num.		perc.
	(km)	(km)	(km)		(%)
1	10.9	11.8	-0.9		-7.6
2	10.9	11.8	-0.9		-7.6
3	11.6	11.9	-0.3		-2.5
4	10.2	12.3	-2.1		-17.1
5	10.1	9.8	0.3		3.1
6	14.9	21.4	-6.5		-30.4
7	26.4	29.5	-3.1		-10.5
8	27.9	29.4	-1.5		-5.1
9	26.5	30.4	-3.9		-12.8
10	24.9	30.4	-5.5		-18.1
11	21.4	30.4	-9.0	†	-29.6
12	20.1	30.4	-10.3	†	-33.9
13	45.6	42.9	2.7		6.3
14	42.3	39.0	3.3		8.5
15	43.0	41.9	1.1		2.6
16	40.3	42.9	-2.6		-6.1
17	35.6	46.0	-10.4	†	-22.6
18	30.4	31.0	-0.6		-1.9
19	22.7	25.7	-3.0		-11.7
20	32.8	25.3	7.5		29.6
21	23.5	27.2	-3.7		-13.6
22	39.4	39.7	-0.3		-0.8
23	20.1	20.3	-0.2		-1.0
24	32.8	30.5	2.3		7.5
25	38.1	40.0	-1.9		-4.8
26	31.1	29.5	1.6		5.4
27	33.6	36.5	-2.9		-7.9
28	27.8	25.0	2.8		11.2
29	24.3	21.2	3.1		14.6

Continued

Table E.2: Statistical Comparison of the Predicted and Seismic Moho Depths. Columns indicate station identification, predicted Moho depth, seismically determined Moho depth, the numeric difference of the two depths (predicted minus seismic), and percentile difference (the raw difference divided by the seismic depth). Depths where the numeric difference was greater than $\pm 2\sigma$ (†) and depths where the percentile difference (num. diff. $\div$ seismic depth) was greater than $\pm 2\sigma$ (‡) are noted. Statistical comparisons excluding no depths, † depths, ‡ depths, and both † and ‡ depths are given at the bottom of the table.

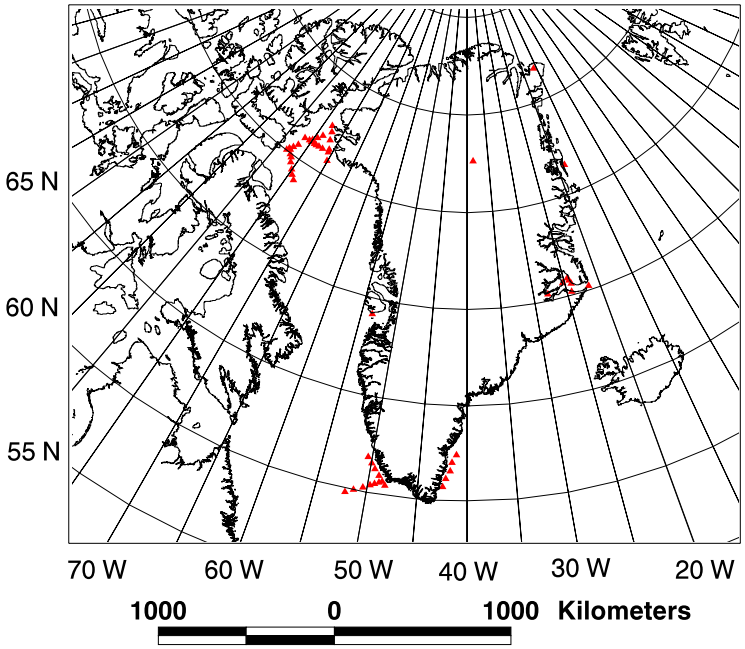

Figure E.3: Location of Greenland control Moho depths listed in Table E.1 and shown in a Lambert Equal-Area Azimuthal Projection centered on 40 W.

Table E.2: Continued

station id no.	DEPTHS predicted (km)	control (km)	DIFFERENCES num. (km)	perc. (%)	
30	38.5	36.0	2.5	6.9	
31	39.1	34.2	4.9	14.3	
32	38.9	32.2	6.7	20.8	
33	25.7	21.0	4.7	22.4	
34	23.1	20.1	3.0	14.9	
35	25.0	17.4	7.6	43.7	‡
36	22.7	16.6	6.1	36.7	‡
37	24.2	17.2	7.0	40.7	‡
38	24.0	20.1	3.9	19.4	
39	20.0	18.9	1.1	5.8	

OVERALL STATISTICAL COMPARISONS: data removed	CC	differences mean	num. RMS	% RMS
none	0.89	0.1	4.6	18.3
† only	0.93	0.9	3.7	17.1
‡ only	0.91	-0.5	4.3	15.1
† and ‡	0.95	0.4	3.4	13.1

to 15.1%. Removal of all 6 stations increases the CC to 0.95, reduces the numeric RMS difference to 3.4 km, increases the mean numeric difference only to 0.4 km, and reduces the percent RMS difference to 13.1%.

E.3 Significance of the quality of the predictions

The removal of these 6 stations (representing about 15% of the total control) significantly improved the overall comparisons. These data are primarily located along the southwestern coastal area and in northern Baffin Bay. The disagreement between the interpolated and seismic values may arise from errors in either or both values. Agreement is taken as an indicator that the Moho model is valid for the other regions.

The excessive errors located areas along the southwestern coast of Greenland appear to more a function of the underlying assumptions than the estimation process or errors in the control data. Examination of Figure E.2 shows that a very pronounced feature extends throughout the region along Greenland's southwestern coast, which intersects the rightmost points in Chian and Louden [1992] survey line shown in Figure E.1.b (corresponding to points 11 and 12 in Table E.2). Chian and Louden [1992] assert that a high density feature exists at this point in their profile and attribute it to possible serpentinized mantle generated during the rifting of Greenland from Labrador. They speculated that the feature may have some lateral extent by comparison with a nearby profile and that it was anomalously high density material as determined by the seismic profiles. If so, then this would be a significant deviation away from the assumption that variations in the Moho depth provide the primary changes in the crustal thickness. Hence, predictions based upon this assumption will produce less desirable results.

Similarly a more regional effect may also be observed along the southeastern coast in Figure E.1.c at the rightmost point [Dahl-Jensen et al., 1998]. Although less pronounced in its sharpness, it also provides a possible deviation away from the underlying assumption for point 17 in Table E.2. Additionally, the locations for the points obtained from Dahl-Jensen et al. [1998] were not given explicitly, (as with Chian and Louden [1992]) but were instead interpolated from their final map. A compass and dividers were used to extract the latitude and longitude information from the projected maps in which Dahl-Jensen et al. [1998] plotted their results. Estimation errors in extracting this location data may shift the actual comparison value interpolated from the Moho grid (Figure E.2).

Similarly, the locations assigned to the measurements from Reid and Jackson [1997] were aslo interpolated from maps. Again, errors in the location determination for points 35, 36, and 37 may have contributed to an erroneous comparison. The locations were re-measured, however, the data were presented in projected coordinates and do not map directly into geographic coordinates.

If these suspect values are disregarded, then the remaining comparisons indicate that the Moho model is reliable to ± 3.4 km. This is less than half the ± 8.5 km standard deviation for Figure E.2. Therefore, the effect of the errors on the Moho depth estimates will be assumed negligible and the Moho model assumed reliable for regional analyses.

E.4 Summary

A Moho undulation grid was predicted using available digital elevation models and assuming an Airy-Heiskanen model of compensation with fixed densities for oceanic and continental regions. Seismic estimates for the depth to the Moho were also available throughout the Greenland area. While no error information was available

with these data, agreement between them and values interpolated off of a predicted Moho undulation grid is assumed to indicate reliability.

There were six stations where the disagreement between the seismic and interpolated depths was more than $\pm 2\sigma$ (i.e., these points fell out side of 95% of the rest of the data). Some of these stations occurred within a region that has been characterized as a possible serpentinized mantle diapir. This represents a deviation away from the uniform density model assumed for the entire Greenland area. Other points may have had there locations inaccurately determined while extracting that data from the maps. Therefore, values interpolated from the final Moho grid may not be correctly related to the seismic estimates.

Discounting the six stations whose locations or underlying assumptions are in doubt, the overall agreement is 95% with agreement at ± 3.4 km or a dimensionless error of 13%. The ± 3.4 km RMS error estimate is less than half the ± 8.5 km standard deviation for the Moho model. The overall agreement between the seismic and interpolated values implies that the predicted grid is reliable for regional analyses.

APPENDIX F

GLQ Geophysical Relationships

The use of Gaussian Legendre Quadrature integration (GLQ) to model the gravitational effect for a prism of rock is well established [von Frese, 1980]. The structural relationships and positions are fixed by assigning the locations of the nodes contained within each prism and the points where the gravity effect of those nodes is desired. A density contrast for the prism is also assumed.

However, performing an inversion based upon GLQ is complicated by the lack of *a priori* knowledge of these positions. Newton's law of gravitation (Equation F.1) indicates that there are two variables that are relevant to the nodes: the volume of the prism and its mass.

$$F = -GM_e \frac{m_{prism}}{l^2} \tag{F.1}$$

where: F = the force of gravitational attraction,
GM_e = the gravitational constant times the Earth's mass,
m_{prism} = $\Delta\rho$·Volume= $\Delta\rho$·height·width·length, and
l = the distance between the source and the observation point

In an inversion, an initial value (1 km) is assumed for the height of the prism. The length and width are determined by the selected latitude and longitude spacing and are fixed, as is the density contrast ($\Delta\rho$). A scale factor is determined and applied to each prism height to generate a prism that will contain sufficient material at the assumed density contrast to generate the gravity values at the observation grid in

a least squares sense. These relationships between the scale factor, height, volume, and, thereby, mass are all linear. The use of a least squares solution necessitates this linear relationship.

However, changing the height value of the grid also changes the physical distance between the source and observation points (l). The linear solution can be applied if the change in node location due to scaling is sufficiently small when compared to the distance between source and observation grids. This is a primary reason for selecting a sufficiently high enough elevation to upward continue free-air gravity anomalies. The trade-off is that the signal attenuates with elevation. Therefore a balance must be struck.

Because the actual relationship is not linear, iterations are required to generate a solution. In each successive iteration, the scale factor should become smaller (if the solution is convergent). Therefore, the subsequent node location changes are smaller, and the effect of this secondary relationship diminishes rapidly.

A simplified example is given in Figure F.1. The simple case where the node is immediately nadir to the the observation point is given, as the primary interest is exemplifying the two relationships between the location and the gravity effect in Equation F.1 and not demonstrating the application of GLQ theory.

As can be seen in Figure F.1, changing nodal height by scaling affects both the volume of the prism (and, hence, mass) and the distance to the observation grid. This secondary change caused by the shift in node location is what necessitates the iterations to generate a complete solution.

There are three factors that can be estimated using GLQ: the gravity effect of the annihilating compensated terrain gravity effect (ACTGE) generated by the density contrast at the Moho, the Moho undulation itself, and the density contrast at the Moho undulation. Use of GLQ to estimate the ACTGE can be represented as a

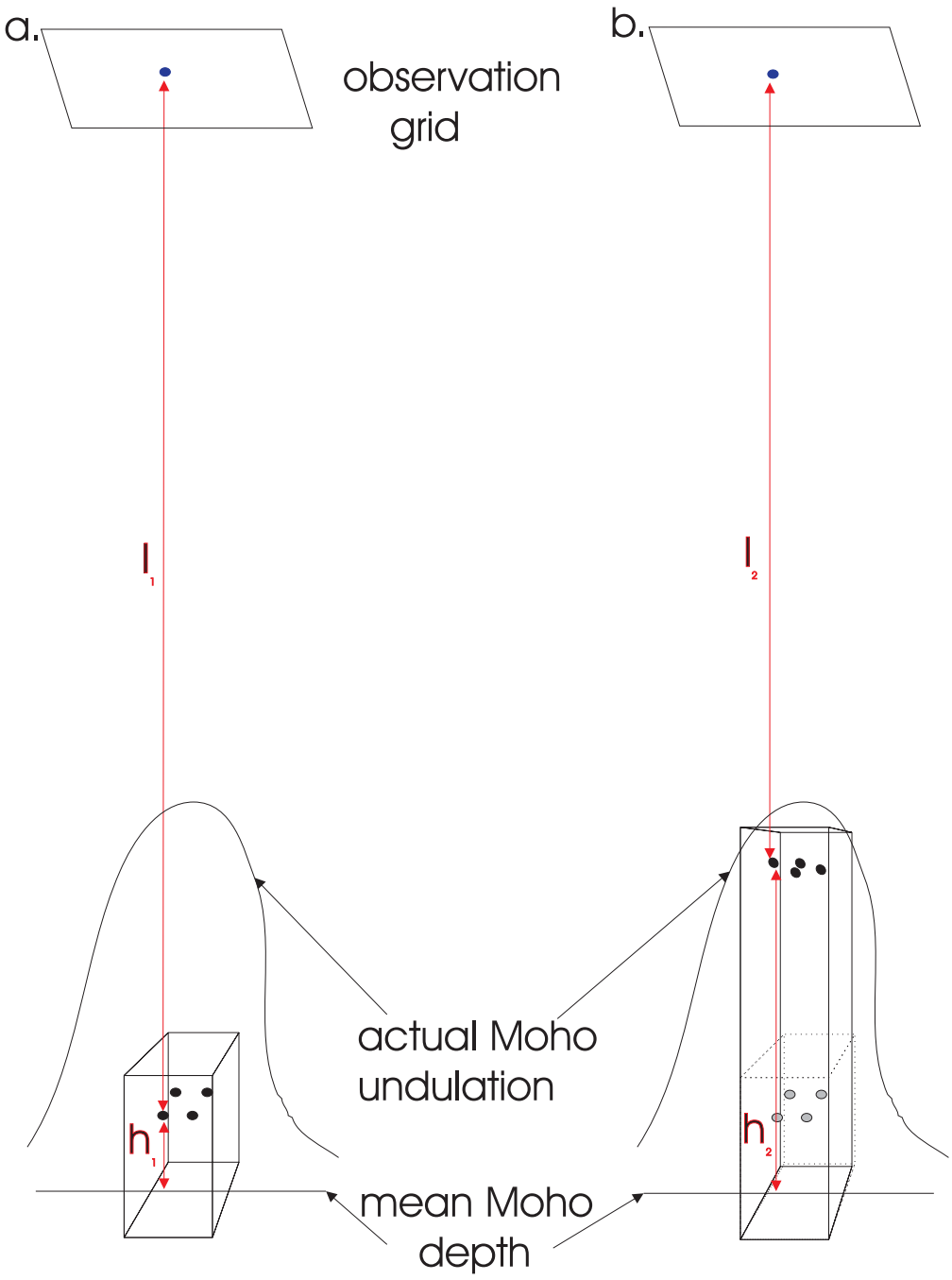

Figure F.1: Depiction of GLQ Geophysical Relationships. **a.** The initial location of the prism, its nodes (black dots), and the observation surface. **b.** The final location of the prism and its nodes. This simplified case depicts the effects on the change of nodal location only for a point immediately above the node in the observation grid. If $h_2 - h_1$ is sufficiently small, then $l_1 \approx l_2$ and the relationship between the prism and the observation points may be linearly modeled.

forward solution, where the Moho undulations are known parameters (x) and are used to estimate the unknown ACTGE values (y) through a design matrix (A) where the densities are fixed (Equation F.2).

$$y = Ax \tag{F.2}$$

Fixing the density contrasts and estimating the Moho from the ACTGE was discussed above and represents an inversion where the unknown Moho depths are the desired parameters ($\hat{x}$) and the observations (y) are used to generate an inverse solution (Equation F.3) using the same fixed densities (A).

$$\hat{x} = (A^t A)^{-1} A^t y \tag{F.3}$$

The final method for applying GLQ is also an inverse solution using gravity values as the observations (y), but the design matrix is different (B) because the Moho depths are fixed and density values for each prism are the desired values (z) as shown in Equation F.4.

$$\hat{z} = (B^t B)^{-1} B^t y \tag{F.4}$$

Once the best estimate for the Moho undulation has been determined from Equation F.3, this method may be now applied to model any residual ACTGE values to modify initial densities using Equation F.4. This permits a more complete modeling of the ACTGE but assumes that the effects of the Moho undulation are the primary source of gravity field variations and density variations are only of secondary concern. If this assumption is invalid, then the resulting predictions may be in error.

However, if later analysis discovers that the initial assumptions about the density contrasts were invalid, the initial models may be updated and new results generated

for the Moho depths. If from the literature or data collection, revised estimates for density in a region become available, these data may be incorporated into the GLQ process. Likewise if reliable depth estimates are available these data may also be incorporated into a solution as constraints ($\breve{x_2}$). A revised model would require that the constraining data be added in accordance with Equation F.5.

$$\hat{x_1} = N_{11}^{-1} A_1^t (y - A_2 \breve{x_2}) \tag{F.5}$$

where: $\hat{x_1}$ = the remaining unknown depths
N_{11}^{-1} = the inversion matrix $(A_1^t A_1)^{-1}$)
A = the design matrix and its two components $[A_1 A_2]$
y = the observation vector
$\breve{x_2}$ = the constraints

Because the new data used as constraints would be replacing old cells, the data must be regenerated.

APPENDIX G

Kinematic Model Summary of Events for Greenland

Srivastava and Tapscott [1986] divided the entire North Atlantic Ocean region and the borderlands surrounding it into 6 major areas when they developed their kinematic model for its opening. Four of these six are relevant to the formation of the Labrador Sea. Table G.1 summarizes the chronological development of these four regions in terms of major geologic events for the past 130 Ma that were adapted from Table 3 of Srivastava and Tapscott [1986].

According to Srivastava and Tapscott [1986], the initial rifting of the North Atlantic started approximately 95 Ma, progressing from the south along the separation of Laurasia and Gondwana. Spreading initially took place in the Rockall Trough just east of the Rockall-Hutton Bank, which was then located off of the southeastern coast of Greenland. The Rockall-Hutton Bank represented a piece of Precambrian terrain that was a part of the South Greenland Archean province [Toft and Arkani-Hamed, 1993; Dahl-Jensen et al., 1998; Vogt, 1986]. At about 84 Ma, seafloor spreading initiated within the Labrador Sea as rifting halted in the Rockall-Hutton Trough. This rifting resulted in the separation of Greenland from North America as Greenland began to move with Europe.

Seafloor spreading in southwestern Greenland caused a counter-clockwise rotation and initiated compression in the northwest with Ellesmere Island in what would

become the Eurekan Orogeny. Initial motion of Greenland from isochrons 33 through 25 (ca. 84 to 60 Ma) was largely in an ENE direction. From isochrons 24 through 21 (ca. 56 to 50 Ma), a 45° shift in spreading direction occurred, such that motion was now mostly N-S as Greenland separated from the Rockall-Hutton Bank and Europe. This change in direction coincided with the separation of the Lomonosov Ridge from the Eurasian continental shelf to the north.

Eventually, the Labrador spreading ridge failed at about isochron 13 (ca. 20 Ma). At that time Greenland began to move with North America and the Eurekan Orogeny halted. From that time to the present, Greenland has been relatively quiescent.

Anomaly	Age (Ma)	Arctic Basin	Greenland-Norwegian Seas
M11	Hauterivian (130)	Opening of the Canada Basin	—
M0	Aptian (118)	Near extinction of spreading in Canada Basin.	—
M0-34	Cenomanian (95)	Initiation of compression between Lomonosov Ridge and on Siberian Platform possibly along Verkhoyansk fold belt.	—
34	Campanian (84)	Some spreading in the Makarov Basin. Compression along Verkhoyansk fold belt.	Rifting in the Greenland-Norwegian Sea.
31	Maastrichtian (68)	Some spreading in the Makarov Basin.	As above.
25	Thanetian (59)	Shearing in the northern Siberian Platform due to separation of Lomonosov Ridge from the Barents Shelf.	Volcanism in eastern Greenland near Scoresby Sund and on the Voring Plateau, Faeroe Islands and initiation of Greenland-Scotland Ridge.
24	Ypresian (56) (E. Eocene)	Dilation in the northern part of the Siberian Platform and compression in the southern part, possibly along Verkhoyansk fold belt.	Active sea-floor spreading in Norwegian and Greenland Seas.
21	Lutetian (50) (M. Eocene)	As above.	Formation of a large part of Iceland-Faeroe Ridge. Possible jump of ridge axis to the west.
13	Rupelian (36) (E. Oligocene)	Shearing motion on Siberian Platform along Leona River.	Sea-floor spreading in Norwegian and Greenland Seas continuing. Simultaneous spreading east and west of Jan Mayan Ridge.
7	Chattian (26) (L. Oligocene)	As above.	Jan Mayan Ridge separates from Greenland and spreading starts Kolbeinsey Ridge. Spreading in the Norwegian Sea and on the Iceland-Faeroe Ridge terminates and starts in Iceland.
0	Present	Strike-slip motion along the intercontinental boundary between Eurasia and North America on the Siberian Platform.	Spreading taking place across Reykjanes, Kolbeinsey, Mohn and Knipovich Ridges and in Iceland.

adapted from Table 3 of Srivastava and Tapscott [1986]

Continued

Table G.1: Chronological summary of tectonic events for the Greenland area. The conventional name of the associated magnetic isochron is given under the "anomaly" heading. Geologic age and associated time in millions of years is given under the "age (Ma)" heading. Subsequent columns for the listed regions summarize the geologic events of their evolution.

Table G.1: Continued

Anomaly	Age (Ma)	Labrador Sea	North Atlantic
M11	Hauterivian (130)	—	—
M0	Aptian (118)	Volcanism on the southern Labrador Shelf and on land associated with the initial stages of sea-floor spreading in the Labrador Sea.	Initiation of rifting between the Porcupine Bank and Orphan Knoll and in the Rockall-Hutton Trough.
M0-34	Cenomanian (95)	Rifting between Greenland and Labrador, volcanism on the outer shelf.	Initiation of active sea-floor spreading in the North Atlantic and Rockall-Hutton Trough (all regions south of the Charlie Gibbs FZ).
34	Campanian (84)	Active sea-floor spreading in the south Labrador sea and rifting in the north Labrador Sea and Baffin Bay. Counterclockwise rotation of Greenland relative to Ellesmere Island and start of compression in the northern Sverdrup Basin.	Active sea-floor spreading in all regions south of Greenland, jump of ridge axis to the west and spreading stopped in Rockall-Hutton Trough.
31	Maastrichtian (68)	Active sea-floor spreading in the north Labrador Sea and rifting in the northern Baffin Bay. Compression in the Sverdrup Basin and start of the Eurekan Orogeny.	Active sea-floor spreading continuing.
25	Thanetian (59)	Volcanism in the Davis Strait and surrounding regions, change in direction of motion between Greenland and North America; Greenland begins to move at an angle to the Nares Strait.	Volcanism forming the Thulean Rise. Formation of the Azores-Biscay Rise.
24	Ypresian (56) (E. Eocene)	Change in direction of motion between Greenland and North America. Oblique spreading in Baffin Bay and Davis Strait resulting in mainly shear motion.	Compression and strike-slip movement along the Iberia-Africa and Eurasian boundary.
21	Lutetian (50) (M. Eocene)	Change in direction of motion between Greenland and North America. Motion between Greenland and Ellesmere Island is mainly compressional.	As above and start of formation of King's Trough.
13	Rupelian (36) (E. Oligocene)	Extinction of sea-floor spreading in Baffin Bay and Labrador Sea. Greenland started to move with North America.	Motion along King's Trough continuing.
7	Chattian (26) (L. Oligocene)	—	Motion along King's Trough stopped. Plate boundary between Eurasia and Africa shifts to the south along the Azores-Gibraltar FZ.
0	Present	—	Spreading taking place across the MAR.

APPENDIX H

Acronym Definitions

ACTGE	Annihilating Compensated Terrain Gravity Effect
AGC	Atlantic Geoscience Centre
ASD	Standard Deviation
BRT	Bottom Relief Topography
CTGE	Compensated Terrain Gravity Effect
DEM	Digital Elevation Model
DLFI	Differenced Local Favorability Indices
FAGA	Free-Air Gravity Anomalies
FVD(CGE)	First Vertical Derivative of Crustal Gravity Effect
FVD(IC-TDFAGA)	First Vertical Derivative of IC-TDFAGA
GAP91	Greenland Aerogeophysical Project 1991
GAP92	Greenland Aerogeophysical Project 1992
GGM	Gravity Geologic Method
GLQ	Gaussian Legendre Quadrature integration
GQLFI	Gravity Quotient Local Favorability Indices
GSC	Geological Survey of Canada
IC-RTPMA	IntraCrustal Reduced-To-Pole Magnetic Anomalies
IC-TDFAGA	IntraCrustal Terrain Decorrelated Free-Air Gravity Anomalies
IGRF	International Geomagnetic Reference Model
LFI	Local Favorability Indices
MA	Magnetic Anomalies
MC-RTPMA	Mantle/Core Reduced-To-Pole Magnetic Anomalies
MQLFI	Magnetic Quotient Local Favorability Indices
MSL	Mean Sea Level
NRL	Naval Research Laboratory
OBS	OBServed
QLFI	Quotient LFI
REG	REGional
RES	RESidual
RTP	Reduced-To-Pole
RTPMA	Reduced-To-Pole Magnetic Anomalies
SLFI	Summed Local Favorability Indices
TCFAGA	Terrain Correlated Free-Air Gravity Anomalies
TDFAGA	Terrain Decorrelated Free-Air Gravity Anomalies
TGE	Terrain Gravity Effect